

**Adventures in atomic force microscopy:
towards the study of the solid-liquid interface**

Aleksander Labuda
Physics Department, McGill University,
Montreal, Québec, Canada.
August 2012

*A thesis submitted to McGill University in partial fulfillment
of the requirements of the degree of Doctor of Philosophy*

All graphs were generated using **MATLAB**,
graphics were created using **CorelDRAW**,
3D figures were made in **Catia V5**,
and this document was formatted using **Microsoft Word**.

“There’s something strangely musical about noise.”

– Trent Reznor

Table of contents

Abstract.....	vi
Résumé.....	vii
Acknowledgments.....	viii
Statement of originality.....	ix
Note about hyperlinks.....	x
1. Introduction.....	1
1.1 Scientific context.....	1
1.2 Technological context.....	2
1.3 Outline.....	3
2. Instrumentation.....	4
2.1 Design of a static atomic force microscope with electrochemical control.....	4
2.2 Design of a dynamic atomic force microscope.....	6
2.3 Noise map for atomic force microscopy.....	7
2.4 Noise limits of optical beam deflection.....	8
2.4.1 Characterization of optical noise.....	8
2.4.2 Derivation of angular detection noise density.....	10
2.4.3 Exploiting cantilever curvature.....	11
2.4.4 Fresnel-patterned cantilever coating.....	13
3. Methodology.....	15
3.1 Signal interpretation in AM-AFM.....	16
3.1.1 Derivation of AM-AFM theory.....	16
3.1.2 Cantilever calibration in overdamped environments.....	17
3.1.3 Limits to piezoacoustic excitation in AM-AFM.....	19
3.2 Signal interpretation in FM-AFM.....	20
3.2.1 Derivation of ideal FM-AFM.....	20
3.2.2 Transfer functions of the AFM system.....	21
3.2.3 Derivation of real FM-AFM in liquid environments.....	22
3.2.4 Limits to piezoacoustic excitation in FM-AFM.....	24
3.3 Stochastic simulation of hydration measurements.....	25
3.3.1 AFM characterization.....	26
3.3.2 AFM simulation.....	27
3.3.3 Noise assessment.....	29
4. Hydration structures of water on mica.....	30
4.1 The electrical double layer.....	30

4.1.1	Statistical mechanics of the EDL	31
4.2	Atomic-resolution hydration experiment.....	33
4.2.1	Three-dimensional force spectroscopy	33
4.2.2	Nanosopic vs mesoscopic hydration experiments	34
4.2.3	Damping in nanoscopic hydration experiment	35
4.2.4	Determination of tip-sample distance.....	37
4.2.5	Summary and outlook.....	39
5.	Solvation structures of ionic liquids at the gold interface	40
5.1	Ionic liquid electrochemical theory.....	40
5.1.1	Statistical mechanics of the ionic liquid EDL.....	41
5.1.2	Differential capacitance of ionic liquids.....	42
5.1.3	Corrections to first order theory	44
5.2	Ionic liquid selection criteria	46
5.2.1	Current scientific arena	47
5.2.2	Experimental feasibility	48
5.3	Cyclic voltammetry	48
5.3.1	The double layer regime	49
5.3.2	The faradaic regime	51
5.3.3	The mass transport regime	52
5.4	Atomic force microscopy	53
5.4.1	Imaging the IL/gold interface	53
5.4.2	Force spectroscopy of the IL solvation structure	54
6.	Conclusions and Outlook.....	57
6.1	Conclusions	57
6.2	Outlook.....	58
7.	Appendix	xi
7.1	Sample preparation	xi
7.1.1	Ionic liquid preparation.....	xi
7.1.2	Au(111) preparation	xi
7.2	Preparation of the instruments.....	xii
7.2.1	Electrochemical studies.....	xii
7.2.2	Atomic force microscopy experiments	xii
7.3	3D interactive technical drawings	xii
8.	References	xiii

Abstract

This thesis presents the design and development of an electrochemical atomic force microscope (AFM) equipped with photothermal excitation for actuation of the cantilever for the study of the solid-liquid interface. A rigorous analysis of noise in the optical beam deflection method is presented and leads to innovative techniques for the reduction of the detection noise to levels well below the thermal noise of the cantilever. An AFM stochastic simulation demonstrates that thermal noise fundamentally limits the measurement of hydration structures at the mica-water interface, whereas tip-sample vibrations may dominate the measurement of the last two hydration layers above the surface. Commonly overlooked problems associated with the traditionally used piezoacoustic excitation are described and quantified with respect to the frequency-modulation (FM) and amplitude-modulation (AM) methods of dynamic AFM operation. After a description of the statistical mechanics of the electric double layer (EDL) of aqueous solutions, a three-dimensional atomic-resolution FM-AFM force spectroscopy experiment of the water-mica interface is presented alongside a detailed analysis of the damping and force profiles used for the determination of the absolute tip-sample distance by comparison to simulations. Lastly, the statistical mechanics of modern ionic liquid EDL electrochemistry are vulgarized, followed by a thorough investigation of cyclic voltammetry of 1-butyl-3-methylimidazolium hexafluorophosphate at the Au(111) interface with comparison to published electrochemical impedance spectroscopy results. The electrochemical observations are complemented by force spectroscopy measurements performed using AM-AFM at different electrode electrochemical potentials across a 2 V window - no relationship between potential and EDL structure was observed.

Résumé

Cette thèse présente la conception et le développement d'un microscope électrochimique à force atomique (AFM) équipé d'excitation photothermique pour l'actionnement du levier pour l'étude de l'interface solide-liquide. Une analyse rigoureuse de bruit dans la méthode de déviation du faisceau optique est présentée et conduit à des nouvelles techniques pour la réduction du bruit de détection à des niveaux en dessous du bruit thermique du levier. Une simulation stochastique d'AFM démontre que le bruit thermique limite fondamentalement la mesure des structures d'hydratation à l'interface mica/eau, tandis que les vibrations mécaniques peuvent dominer la mesure des deux dernières couches d'hydratation au dessus de la surface. Des problèmes couramment négligés associés à l'excitation piezoacoustique traditionnellement utilisée sont décrits et quantifiés par rapport à la modulation de fréquence (FM) et à la modulation d'amplitude (AM) des méthodes de l'AFM en mode dynamique. Après une description de la mécanique statistique de la double couche électrique (EDL) de solutions aqueuses, des mesures de spectroscopie de force de l'interface mica-eau acquises en mode FM-AFM en trois dimensions sont présentées à côté d'une analyse détaillée des profils d'amortissement et de la force utilisée pour la détermination d'une distance absolue entre la pointe et l'échantillon par comparaison à des simulations. Enfin, la mécanique statistique de l'électrochimie ionique moderne est vulgarisée, suivie d'une enquête approfondie de la voltampérométrie cyclique du 1-butyl-3-méthylimidazolium hexafluorophosphate près de l'interface du Au(111) avec comparaison avec les résultats publiés de spectroscopie d'impédance électrochimique. Les observations électrochimiques sont complétées par des mesures de spectroscopie de force réalisée à l'aide d'AM-AFM à différents potentiels électrochimiques d'électrodes à travers une fenêtre de 2 V - aucune relation entre la structure et le potentiel EDL n'a été observée.

Acknowledgments

In alphabetical order:

a. Supervisors

Roland Bennewitz, Peter Grütter, Steve Kecani, and Hirofumi Yamada.

b. Collaborators

Jeffrey Bates, Tiberius Brastaviceanu, Lynda Cockins, Nitya Nand Gosvami, Florian Hausen, Daniel Kiracofe, Kei Kobayashi, Bruce Lennox, Martin Lysy, Yoichi Miyahara, William Paul, Ivan Pavlov, Brendan Pietrobon, Dilson Rassier, Antoine Roy-Gobeil, Mark Sutton, and Kazuhiro Suzuki.

c. Colleagues

Sarah Burke, Jon Buset, Francois Castonguay, John David, Ben Drevniok, Jorge Dulanto, Philip Egberts, Mehdi El Ouali, Tobin Filleter, Shaun Fostner, Ann-Lauriene Haag, Till Hagedorn, James Hedberg, Hadi Izadi, Jeffrey LeDue, Monserratt Lopez, Yoshihiko Nagai, David Oliver, Antoni Tekiel, Jessica Topple, and Chris Voyer.

d. Technical support

Eddie Del Campo, Robert Gagnon, Mario Della Neve, Leo Nikkinen, Richard Talbot, and John Smeros.

e. Funding Agencies

FQRNT, NSERC, and RQMP.

f. Parents

Małgorzata i Damian Labuda.

Statement of originality

- The design and development (mechanical, optical, and electronic) of an electrochemical atomic force microscope (ECAFM) that led to the first-published atomic-scale resolution friction force maps in liquid environments. *Published in [1,2].*
- The design and development (mechanical and optical) of a photothermal excitation system for the ECAFM that led to the first-published stiffness and damping profiles of ionic liquids at the solid electrode interface. *Published in [3].*
- The identification that the curvature of the cantilever plays a role in the detection noise of an optical beam deflection system, and a method for substantially reducing the detection noise. *Published in [4]. Provisional US patent [5].*
- The identification that the excitation transfer function of the piezoelectric transducer used to vibrate the AFM cantilever causes artifacts in the measurement of dissipation processes in FM-AFM in liquid environments, a theory to describe the observations, and a method for correcting the problem. *Published in [6].*
- The identification that the gold coating on a cantilever couples low-frequency light fluctuations into measurable force noise of the cantilever, as well as the demonstration that a patterned coating can reduce both force noise and detection noise in static and dynamic AFM. *Published in [7].*
- The derivation of a simple model for cantilever dynamics in overdamped environments necessary for performing quantitative measurement using dynamic AFM in highly viscous liquids. *Published in [8].*
- The development of a method for stochastic simulation of AFM experiments that includes effects of non-parametric measured power spectral density of instrumental vibrations. *Published in [9].*
- The first atomic-resolution force spectroscopy in liquids performed with accurate dissipation measurements. *Manuscript in publication [10].*

- The design and development (mechanical, optical, and electronic) of an optical beam deflection system for measuring cantilever deflection parallel to a surface, such as a microscope slide. *Published in* [11]. *US patent* [12].
- The identification that the excitation transfer function of the piezoelectric transducer used to vibrate the AFM cantilever causes severe artifacts in the measurement of dissipation processes in FM-AFM in vacuum and cryogenic environments. *Published in* [13]. *Provisional US patent* [14].
- The investigation of the statistical properties of different noise sources in AFM, and the development of a method for accurate integration of the power spectral density for the prediction of variance of linear measurements. *Published in* [15].
- The derivation of a theory that predicts and quantifies the coupling of frequency noise in FM-AFM into amplitude noise that is detrimental to studies of dissipation processes in all environments. *Manuscript in preparation* [16].

Note about hyperlinks

Please note that hyperlinks throughout this document are not replacements for references, and refer only to additional information that is not essential for the integrity of this thesis. Certain hyperlinks lead to online calculations that may benefit readers interested in the exact mathematical steps taken to arrive at a presented result. Some hyperlinks lead to movies that provide additional data to the reader. Other hyperlinks are included in this document for convenience, in case the reader is not familiar with the particular concept for which the link is provided. The latter type of hyperlink typically leads to a Wikipedia article that was deemed adequate for providing additional information regarding the topic at hand.

1. Introduction

1.1 Scientific context

The peculiar nanoscale structure of bulk water that results in its anomalous macroscopic properties, such as the non-monotonic temperature-dependence of density, specific heat and compressibility, continues to be the topic of heated debate [17]. A universal model that accurately describes water on the molecular level is still sought after. Naturally, if the structure of bulk water itself is controversial, the hydration structures around complex proteins are even further from understood. Yet, these hydration structures govern the biomolecular interactions in all living organisms. Molecular dynamics simulations shed light on this problem, but validation by experiment is a necessary step in the process. The construction of more accurate models describing the dynamics and interaction potentials of water molecules are best confirmed by comparison with well-understood systems, rather than complex molecules. The mica surface represents a good candidate for this task as its structure is well understood, and it can be cleanly and reliably prepared in a laboratory setting. Furthermore, the atomic-scale texture of the mica surface templates an intricate, yet repeatable, three-dimensional distribution of water molecules, as proposed by numerous molecular dynamic simulations [18,19]. Although the water-mica interface has been studied by many experimental methods, such as X-ray reflectivity [20] and surface force apparatus [21], atomic force microscopy (AFM) carries the advantage of three-dimensional atomic-scale resolution [22]. This can provide complementary information to strengthen our understanding of the molecular distributions and mechanical properties of water molecules near solid interfaces.

Emerging research in ionic liquids for application in energy-storage technology is motivated by their wide electrochemical windows (~ 5 V), and their promise of producing “green” devices mainly due to their negligible vapour pressure and their chemical stability [23]. Ionic liquids (ILs) are complex organic salts whose ions are poorly coordinated, which prevents the formation of a solid crystal lattice at room-temperature. They can be used as electrolytes for batteries in applications where high energy density is required, or for electrochemical supercapacitors when high specific power is needed. Yet, electrochemical theory of ILs is in its infancy. Whereas interest in IL electrochemistry has been steadily rising for 15 years, the first theories that could explain seemingly-contradictory electrochemical observations only emerged in 2007 [24–26]. The dilute-approximation theory of ionic solutions used throughout the

last century in aqueous electrochemistry qualitatively fails to describe phenomena observed in ILs, even in the low-potential limit. The absence of a solvent that screens charges leads to a system where adjacent charges are strongly correlated. ILs require more elaborate theories derived from the statistical mechanics of dense Coulomb systems because they are inherently saturated ionic solutions. Even then, these mean-field theories are merely a starting point: they do not predict the oscillatory charge profiles which emerge in ILs near solid boundaries, and cannot account for the physicochemical dynamics of IL molecules that strongly influence their electrochemical behavior. Creating an accurate atomistic view of IL electrochemistry requires the consolidation of results between multiple experimental techniques and theoretical modeling. Experimentally, the structure of the electric double-layer of ionic liquids is studied by a variety of electrochemical [27–29] and photochemical [30–32] methods, which measure properties averaged over macroscopic or microscopic electrode areas. AFM provides a complimentary channel of information about the solid-liquid interface which can be used to verify proposed theoretical models [33–35], and carries the advantage of probing nanoscopic areas with characterizable electrode roughness and crystallographic orientation. In this respect, AFM results are relevant for comparison to molecular dynamic simulations [36,37] which are restricted to nanoscopic volumes with well-defined electrodes.

1.2 Technological context

Since its invention over two decades ago, atomic force microscopy (AFM) has branched into numerous techniques and explored environments ranging from ultra-high vacuum (UHV) pressures, milliKelvin temperatures, and liquid environments. Atomic-resolution has proven to be most difficult in liquid environments, where thermal drift, viscous damping, and contamination present some of the largest obstacles. Nevertheless, atomic-resolution was achieved in 2005 by frequency modulation (FM) AFM on a dedicated system with reduced detection noise [38], and now has become routine using amplitude modulation (AM) AFM - but only on the finest commercial AFM [39]. More recently, three-dimensional (3D) force spectroscopy has become possible by further reduction of detection noise in cantilever deflection sensing [22]. The additional reduction of mechanical, thermal and detection noise sources in AFM remains a key factor for enabling faster and more reliable atomic-scale imaging in liquids.

Surpassing these technical hurdles, and achieving high-resolution imaging, naturally precipitates a series of outstanding questions regarding the interpretation of the

acquired FM-AFM and AM-AFM data. These questions conjure controversies in the AFM community as instrumental artifacts are commonly mistaken for physical phenomena occurring between the tip and the sample [40–42]. Liquid AFM theory mainly crutches itself on UHV AFM theory, derived and validated across two decades in its field. Many of the assumptions used in its derivation break down in liquid environments, explaining some of the discrepancies.

Lastly, it is becoming increasingly evident that quantitative AFM using cantilevers that are piezoacoustically excited in liquids is difficult [43], and even impossible in certain cases [6]. Meanwhile, in the UHV community, certain controversies in FM-AFM dissipation measurements have remained unresolved until just recently [13]. These uncertainties inevitably caused misinterpretation of liquid AFM dissipation data as well. Active research is currently seeking more reliable methods and theories for accurate measurements in liquid environments, where instrumental artifacts abound.

1.3 Outline

The instrumentation section describes the particular design and development of the AFM with a sealed electrochemical environment aimed at high-resolution friction force microscopy, followed by a description of the retrofit that enables dynamic AFM by photothermal excitation. Then, an investigation of noise in AFM is presented, the limits of the optical beam deflection method are analyzed, and technological advances are proposed for reducing these limits of detection.

The methodology section deals with accuracy in dynamic AFM. Specifically, the relationship between measured observables and stiffness/damping of the interaction is derived in the context of AM and FM-AFM after careful modeling of the AFM system. The limitations of piezoacoustic excitation are discussed in light of both methods.

The hydration structures of water on mica are studied in the following section. The electric double layer (EDL) theory is derived. Data acquired by atomic-scale 3D force spectroscopy is thoroughly analyzed to extract the damping occurring at the tip apex, and the results are compared to simulations to determine a true tip-sample distance.

The study of solvation structures of ionic liquids at the gold electrode starts by extending the EDL theory from dilute solutions to fully saturated ionic solutions. The solid-liquid interface is first investigated by cyclic voltammetry and carefully compared to recent results in literature, followed by imaging and force spectroscopy using electrochemical AFM.

2. Instrumentation

2.1 Design of a static atomic force microscope with electrochemical control

The scanning of a cantilever tip across a sample with atomic-scale precision requires a very rigid mechanical connection. It may be surprising to some that a mechanical loop with a length on the order of centimeters that connects the tip to the sample can provide the sub-angstrom stability necessary for atomic-scale resolution. As a [back-of-the-envelope calculation](#), take an aluminum bar with a $1\text{ cm} \times 1\text{ cm}$ cross-section and a length of 10 cm, and shape it into a “C” where the ends are nearly touching. A [simple shear calculation](#) provides the lateral stiffness relating the two ends: $\sim 3 \times 10^7\text{ N/m}$. The equipartition theorem predicts vibrations on the order of 10 fm between the ends of such a mechanical loop for the fundamental vibration mode. Clearly, aluminum is stiff enough to construct a tip-sample junction. However, in practice, this thermal vibration limit is overshadowed by external noise coupling. This aluminum “C” has a high mechanical Q factor and a resonance frequency of a few kHz, which is problematic since atomic force microscopy measures forces on corresponding time scales. Consequently, great care must be invested into stiffening the tip-sample junction in order to increase its resonance frequency and to reduce its response to external forces. Importantly, the mass coupled to the mechanical loop should be minimized to maintain a high resonance frequency.

A certain minimum mass is necessary to accommodate the optics, electronics, and mechanics necessary for the detection of the cantilever deflection. However, because the displacement of the cantilever tip is amplified by more than $100 \times$ (\sim effective focal length/cantilever length) before the light beam reaches the photodetector, vibrations in the detection mechanics have less than $100 \times$ the impact on the measured signal. This allowance permits the design of large and heavy (nevertheless rigid) detection optomechanics. It is however crucial to mechanically decouple the detection assembly from the tip-sample junction to prevent mass loading as described in the previous paragraph.

These considerations served as a basis for the design of our AFM, illustrated in Figure 1. The coarse positioning of the tip relative to the sample is enabled by three $\frac{1}{4}$ -80 TPI screws that rotate against three ball bearings. The assembly is spring-loaded to increase the radial and axial stiffness of the ball bearings. The remainder of the mechanical loop comprises of a glass rod, bulk aluminum, and a piezoelectric tube used for sample positioning. The detection optomechanics are packaged inside the large optical head,

which mechanically grounds the optical fiber and electronic connections to reduce their impact on tip-sample vibrations.

The second fundamental design consideration lies in the electrochemical purity of the liquid cell. The liquid is injected into the cell through Teflon [PFA](#) tubing. The solution contacts the [PEEK](#) walls of the cell, as well as the quartz rod which is used to both guide the detection light beam into the cell and to hold the silicon cantilever. All these materials are reputed for their electrochemical purity, absence of leaching compounds such as [phthalates](#), and resistance to nearly all solvents which allows efficient cleaning in between experiments. Gold is used as the working electrode (WE) and counter electrode (CE) material, along with an Ag/AgCl leak-free reference electrode (RE). A mechanically compliant Teflon [FEP](#) foil forms the floor of the liquid cell, isolating the piezoelectric tube underneath which moves the sample in three-dimensions. An encapsulated magnet within the sample binds it to the piezoelectric tube, without ever making contact with the liquid.

This outlines the key design considerations that led to successful atomic-scale lateral force images with electrochemical control presented in Figure 2. These results were published in [1] and [2].

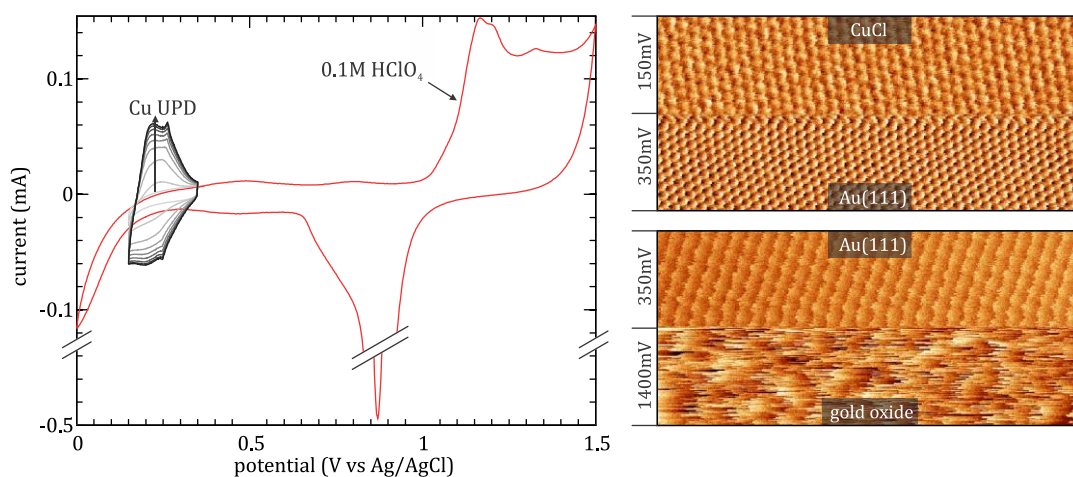
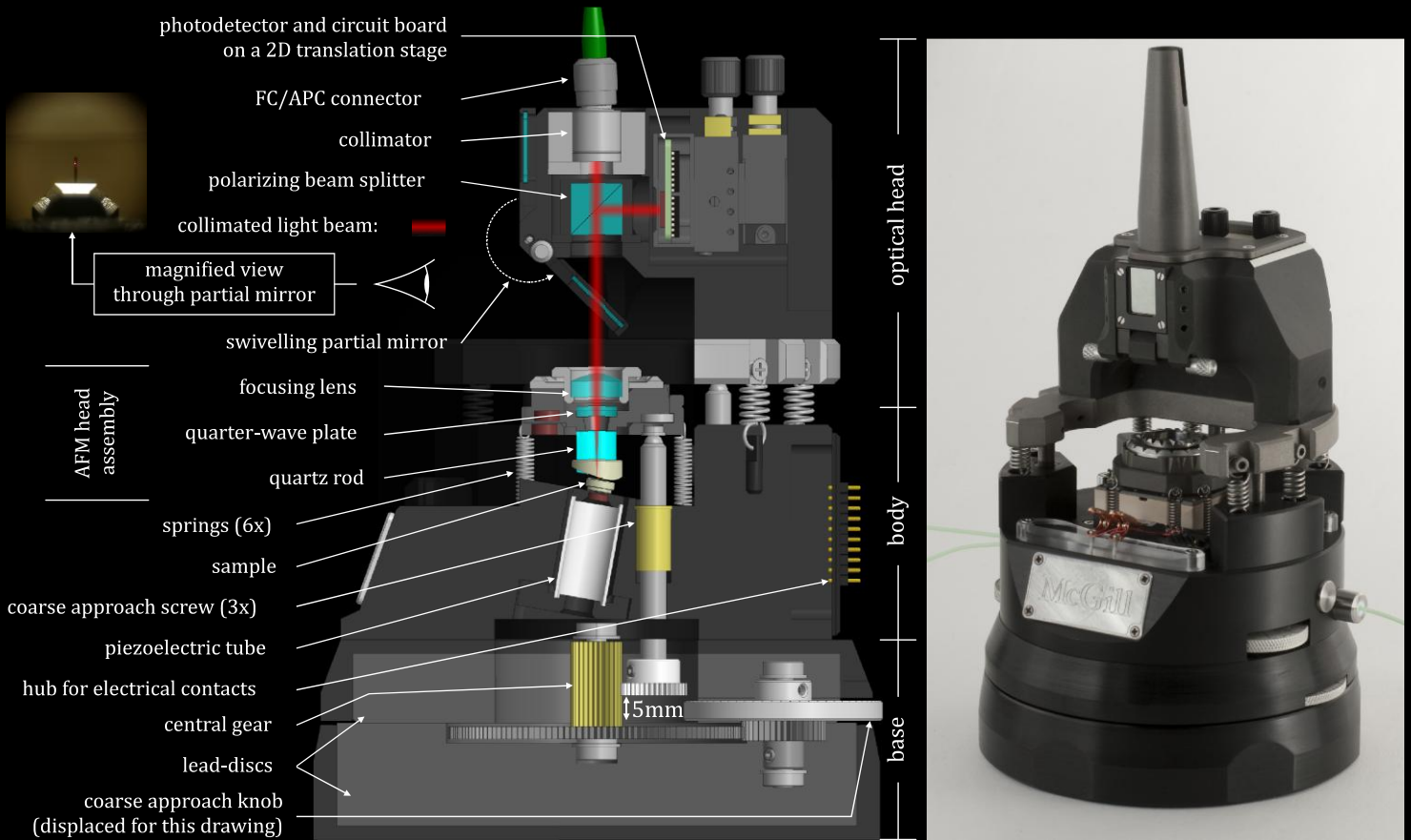


Figure 2: (left) Cyclic voltammogram of *in situ* Au(111) in 0.1 M perchloric acid, and during the injection of copper perchlorate that undergoes under-potential deposition (UPD). Switching the potential between 150, 350, and 1400 mV leads to CuCl, Au(111), and gold oxide surfaces, respectively, as shown on the atomic-scale lateral force maps (right). The images represent the lateral force on the tip as it slides by stick-slip motion across the surface. Note that the scales are different for both images; the lattice constant of Au(111) is 0.29nm.

a) side view technical drawing and photograph of the ECAFM



b) technical drawing and photographs of the AFM head and the electrochemical liquid cell

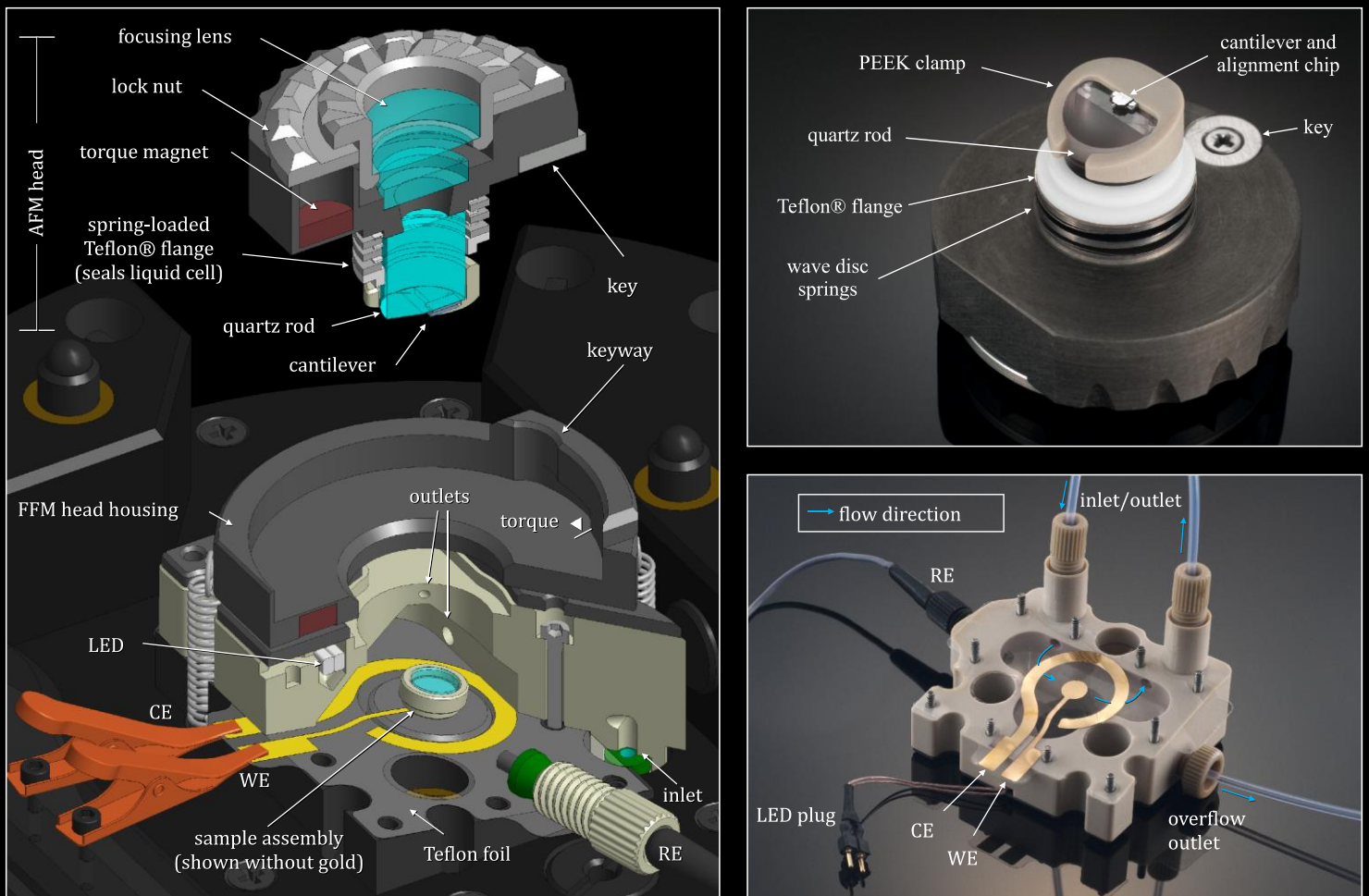
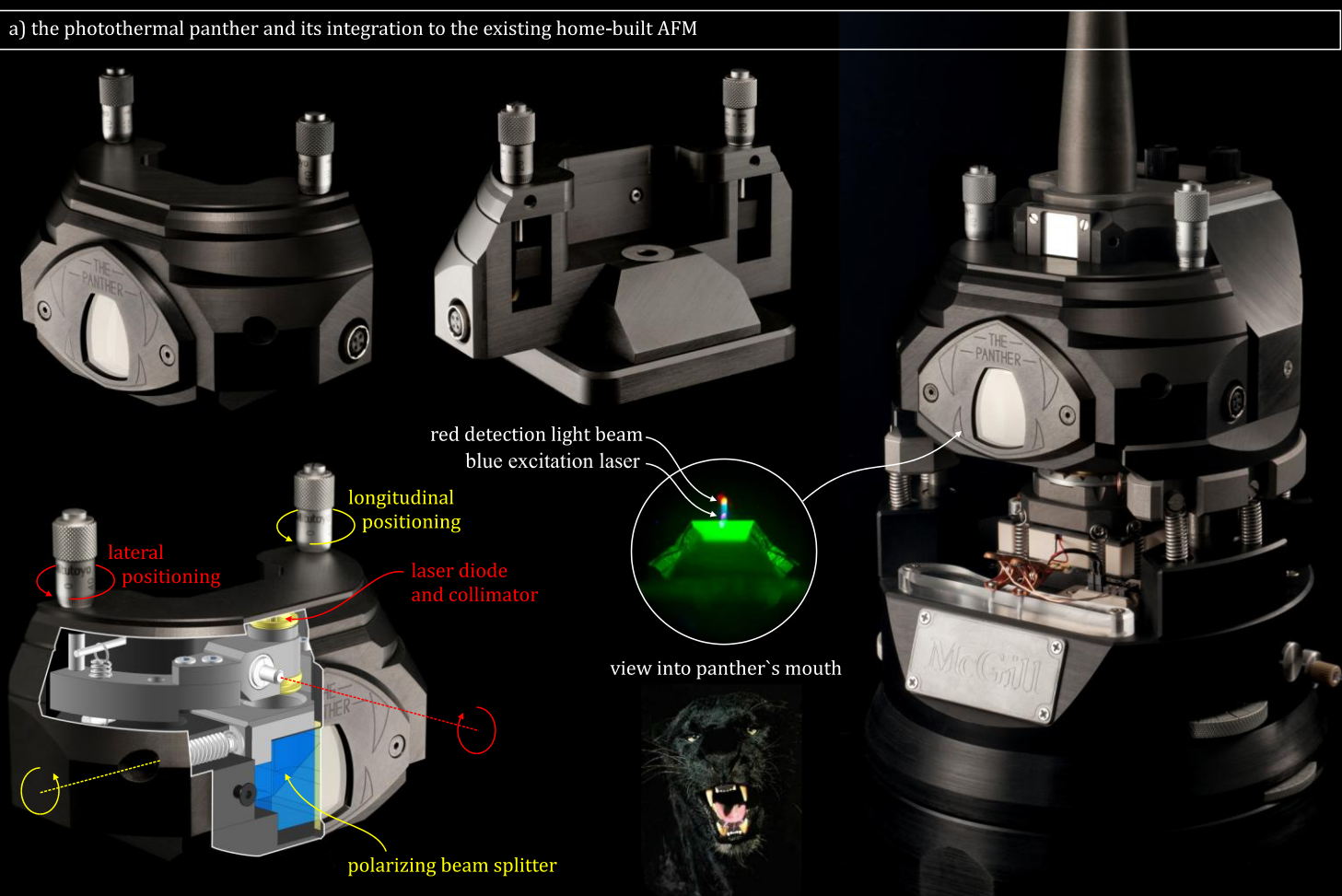
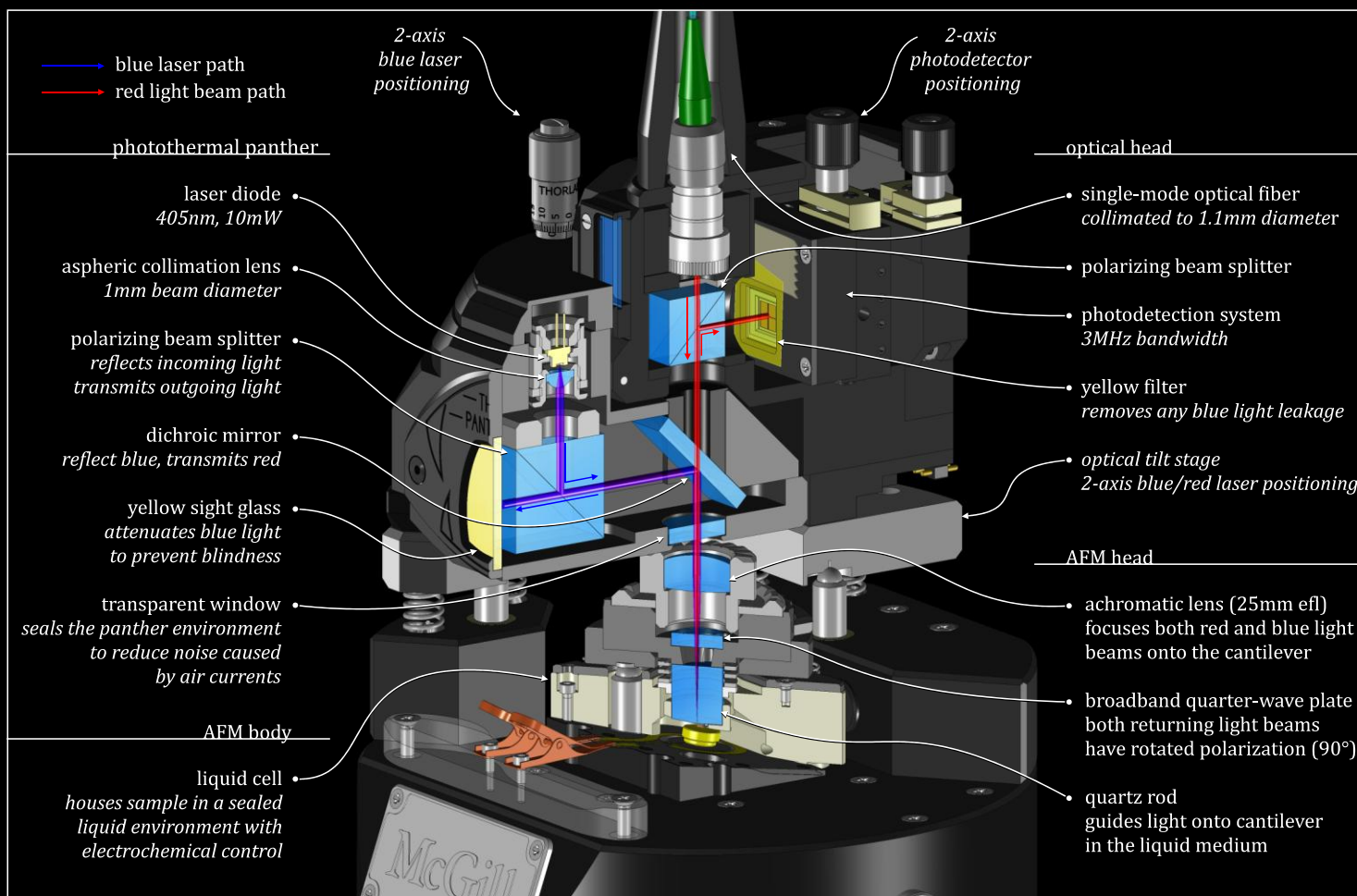


Figure 1: Technical drawings and photographs of the electrochemical atomic force microscope. a) General outline of the design. b) Details regarding the electrochemical liquid cell. RE: reference electrode. CE: counter electrode. WE: working electrode.

a) the photothermal panther and its integration to the existing home-built AFM



b) summary of optical components



2.2 Design of a dynamic atomic force microscope

The same design principles outlined in the previous section apply to the design of a dynamic AFM, which uses a sinusoidally driven cantilever to probe surface interaction forces. However, the requirements for a stable detection assembly are even less demanding because the cantilever deflection signal is demodulated from a high frequency. Therefore, all optomechanical vibrations occurring away from the cantilever resonance frequency are filtered and therefore can be ignored. This relaxed condition greatly simplified the design considerations when retrofitting the static AFM (described in the previous section) with dynamic AFM capabilities. The retrofit nearly doubled the mass of the optical head used for detection and includes a thick cable which may couple external vibrations to the optomechanics, without concern.

Figure 3a depicts the photothermal excitation unit, dubbed “the panther”, which magnetically mounts to the existing optical head and incorporates a blue laser (405 nm) for cantilever excitation. The blue laser power is modulated by a laser diode driver designed and built by Kei Kobayashi. This optical power modulation transduces into a time-varying thermal stress of the cantilever causing it to oscillate sinusoidally.

The blue laser can be positioned onto the cantilever by two micrometer screws providing micron positioning sensitivity. A dichroic mirror combines the blue excitation laser to the existing red detection light beam. Both light beams are collimated and share the same achromatic lens, and therefore are coincidentally focused onto the cantilever. The panther’s mouth provides a view of a green cantilever, with highly dimmed red and blue light beams which can be positioned onto the cantilever by visual inspection.

Figure 4 shows the performance of the system for the excitation of a cantilever in water. The design of the photothermal panther was published in [3].

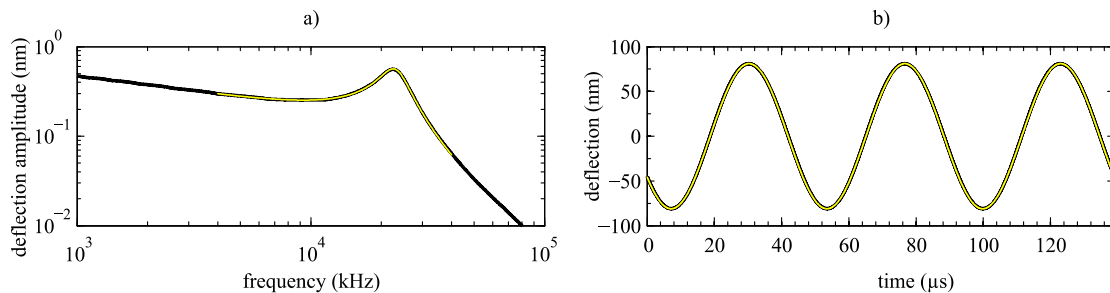


Figure 4: a) The photothermally driven cantilever amplitude response in water far from the surface. Cantilever stiffness: 1.34 N/m; and Q : 3.6. A harmonic oscillator function with $1/f$ background is fit and overlaid. b) Driving the cantilever on-resonance demonstrates the linearity of the system up to large oscillation amplitudes. A sinusoidal function was fit and overlaid. The residual plot deviates by no more than 0.3 % of the oscillation amplitude (not shown).

2.3 Noise map for atomic force microscopy

Noise sources in atomic force microscopy are abundant. To add insult to injury, they can vary from one day to the next, or from minute to minute, for countless reasons. Characterizing the noise of an AFM not only serves as a tool for designing a better instrument, but also provides a roadmap for troubleshooting intermittent problems from a day-to-day operational stand-point. Furthermore, proper noise characterization can be used to compare different instruments with respect to their expected performance for specific experiments, as will be demonstrated later.

The noise map in Figure 5 provides a visual representation of the main noise sources in a typical AFM, and establishes the nomenclature that will be referred to throughout this thesis. The phenomenological classification of noise into three categories was described in [7]: detection noise, displacement noise and force noise. An example of the spectral density of these noises is shown in Figure 6.

All three noises affect the outcome of experiments very differently, yet they may not be readily distinguishable. For example, our optical beam deflection system has no 60 Hz detection noise, however the cantilever vibrates at 60 Hz and harmonics due to coupling with light power fluctuations. These observable vibrations are counterintuitively classified as force noise, not detection noise. Both of these noises are discussed in the following subsections, whereas displacement noise (tip-sample vibrations) was the topic of Section 2.1.

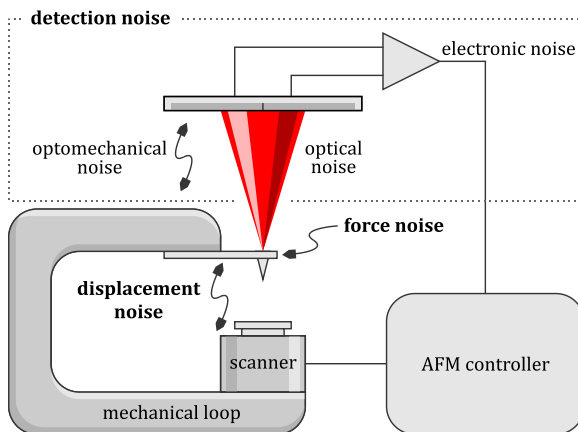
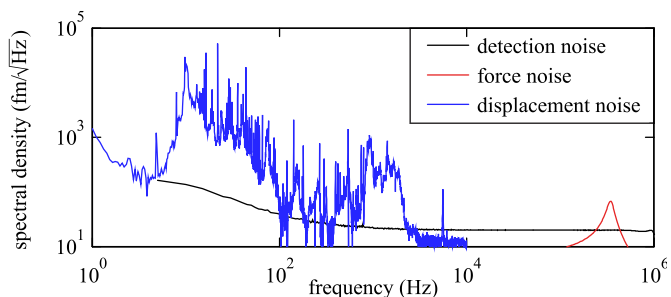


Figure 5: The cantilever and sample are connected by a mechanical loop that can vibrate and cause **displacement noise**. The cantilever can be subject to thermal and mechanical disturbances causing **force noise**. The **detection noise** is a combination of optomechanical vibrations, optical fluctuations inherent to the light beam (in red), and additional electronic noise

Figure 6: An example of detection noise measured by reflecting the light beam off the rigid cantilever base; force noise modelled as the thermal noise of a hydrodynamic oscillator [44]; and displacement noise measured on our AFM (the detection noise was subtracted)



The detection of angular deflections of the cantilever is limited by the performance of the optical beam deflection (OBD) system. As described in section 2.1, the mechanical stability requirements for the OBD detection system are much more relaxed than for the tip-sample junction because they do not contribute to displacement noise. Despite the large weight of the optical head, our OBD system has no measurable optomechanical vibrations, and the electronic noise is made negligible with respect to the optical noise across the 3 MHz bandwidth of the instrument; this was achieved by appropriate electronic design described in [1]. This section investigates the optical noise that dominates the detection noise of the OBD system, and presents methods for reducing its impact on cantilever deflection measurements.

2.4.1 Characterization of optical noise

The fundamental limit to optical noise is shot noise. Shot noise is caused by the discrete nature of photons that arrive at the photodetector with random inter-arrival times. Because the quantum efficiency of our photodetector¹ is close to 1 e⁻/ph, the optoelectronic and optical shot noises (discrete electrons vs discrete photons) will not be distinguished here for the sake of discussion.

The optical shot noise density can easily be calculated for a 1 mW light beam, by²

$$n_{shot}(f) = \sqrt{\frac{2}{3.4 \times 10^{15} \text{ ph/sec}}} = 2.4 \times 10^{-8} / \sqrt{\text{Hz}} \quad (1)$$

where the factor of 2 is introduced because of the convention of folding negative frequencies onto positive ones (*i.e.*: single-sided power spectral density). This noise density represents the fraction of the light beam that is undergoing fluctuations for a given unit bandwidth. For a 1 second measurement, the optical power can be determined up to an error of 24 parts per billion, or 24 pW.

This high level of precision is completely trumped by additional noise sources. Excess noise, for example, is another fundamental noise source which affects superluminescent diodes [45] and exceeds shot noise by an order of magnitude for our light beam.

¹ Inspection of the datasheet ($\eta = 0.468 \text{ A/W}$) and subsequent calculation ($\xi = h\nu/e\eta$) resulted in a quantum efficiency $\xi = 0.86 \pm 0.01 \text{ e}^-/\text{ph}$ at 679 nm.

² The well-known relative standard deviation $\sigma = 1/\sqrt{N}$ of a Poisson random variable takes on a time-dependence by reparameterization $N(t) = \lambda t$, where λ is the rate in events/sec, defined by the spectral density $n = \sigma\sqrt{t} = 1/\sqrt{\lambda}$.

Furthermore, electronic noise of our current source causes yet another order of magnitude more noise above excess noise. These noise sources appear in the sum signal

$$\Sigma(t) = \frac{P_B(t) + P_A(t)}{P_0} \quad (2)$$

where the sum of the instantaneous light power on each photodetector side (P_A and P_B) is normalized by the time-averaged light power P_0 . The noise density of the sum signal $\Sigma(t)$ is termed “common-mode” noise $n_{CM}(f)$ and is shown in Figure 7a, where it exceeds shot noise by two to three orders of magnitude.

However, these additional common-mode noise sources are spatially correlated, such that they affect the light on both sides of the photodetector equally. As long as the light beam is perfectly centered onto the photodetector, the difference

$$\Delta(t) = \frac{P_B(t) - P_A(t)}{P_0} \quad (3)$$

is practically impervious to these noise sources. In this situation, the noise density of the difference signal $\Sigma(t)$ is termed “differential-mode” noise $n_{DM}(f)$ and is shown in Figure 7a. Shot noise defines the fundamental limit of differential-mode noise as it is spatially uncorrelated. Below 100 Hz, $1/f$ noise dominates the difference signal.

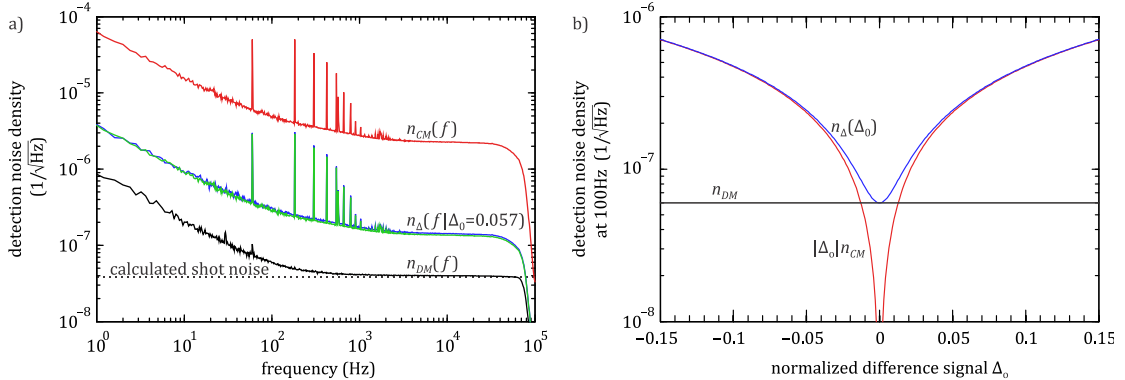


Figure 7: a) Differential-mode n_{DM} and common-mode noise n_{CM} are measured when the light beam is centered on the photodetector. They can be used to predict the detection noise n_{Δ} at any position of the light beam on the photodetector, defined by the time-averaged difference signal Δ_0 . The predicted and measured detection noises n_{Δ} overlay perfectly. b) The detection noise density at 100 Hz is plotted as a function of Δ_0 . Note that 60 Hz and harmonics only affect the common-mode noise, and not the differential mode-noise.

During an AFM experiment, the light beam does not necessarily remain perfectly centered on the split photodetector (used to measure cantilever deflection) throughout the experiment. In a static AFM experiment, changing the force setpoint results in a light beam that is off-centered. However, the two previous noise measurements, n_{CM} and n_{DM} , suffice for determining the optical detection noise density $n_{\Delta}(f|\Delta_0)$ in situations where the light beam is off-centered, and can be computed by [15]

$$n_{\Delta}^2(f|\Delta_0) = n_{DM}^2 + |\Delta_0|^2 n_{CM}^2 \quad (4)$$

where Δ_0 is the time-averaged value of $\Delta(t)$. The validity of this equation, which is actually an approximation³, is verified in Figure 7a where the predicted value $n_{\Delta}(f|\Delta_0 = 0.57)$ overlays the measured value impeccably.

In our AFM, using 450 μm long cantilevers with stiffness of 0.1 N/m, the common-mode noise exceeds the differential-mode noise as soon as the normal force > 15 nN. Alternatively, the common-mode noise may dominate at zero force if the light beam is not perfectly centered at the start of the experiment, for both static and dynamic AFM operation. Figure 7b demonstrates how the difference signal noise density changes as a function of the time-averaged difference signal Δ_0 .

2.4.2 Derivation of angular detection noise density

In the previous section, the optical noise of the light beam was characterized in its collimated state and shining directly onto the photodetector. The detection noise density $n_{\Delta}(f)$ has units of $1/\sqrt{\text{Hz}}$ as it represents the fractional noise of a light beam. This noise will now be assigned units of radians to determine its limits in detecting *angular* deflections of the cantilever.

To a very good approximation, the photodetector is positioned in the far-field in an AFM. The far-field represents distances (from the light beam focus) large enough that the beam can be approximated as a cone emanating from a point source. Even a perfectly collimated 2 mm laser pointer has a far-field, which begins at 10 meters. Because cantilevers are microscopic, AFM light beams are focused to small diameters, usually $2w_0 \leq 50 \mu\text{m}$. Therefore the [Rayleigh range](#) z_R , which delimits the start of the far-field, becomes $z_R < 1.2$ cm in AFM, and the detection light beam can be approximated as a cone of light with its origin at the cantilever and a divergence angle $\phi = \lambda/(\pi w_0)$. The cantilever deflects this cone, and the photodetector measures the deflection angle. As shown in Figure 8a, the light beam acts as a protractor.

The divergence angle of the reflected light cone naturally determines the range of measurable angles as demonstrated in Figure 8b (assuming the photodetector is not the limiting factor). For a Gaussian beam, the maximum range of angles θ_{max} is related to the divergence ϕ_{out} by a factor:

³ This equation holds when the fraction of the light on either photodetector $\left(\frac{P_A}{P_A+P_B}\right)$ and the total light $(P_A + P_B)$ are independent. While this equation is not expected to be strictly true, it can be a good approximation in practice.

$$\theta_{max} = \frac{\phi_{out}}{4} \sqrt{\frac{\pi}{2}}. \quad (5)$$

The detection noise density $n_{\Delta}(f)$ is independent of the beam divergence or spot size on the photodetector, such that the angular detection noise density $n_{\theta}(f)$, in units of rad/\sqrt{Hz} , can be determined by the product

$$n_{\theta}(f) = \theta_{max} \times n_{\Delta}(f). \quad (6)$$

In other words, $n_{\Delta}(f)$ defines the fraction of the angle θ_{max} which contributes to noise, per unit bandwidth.

This implies that the angular detection noise, which defines the lower limit of detection of an OBD system across any arbitrary bandwidth, is proportional to the divergence angle of the reflected light beam. It is important to note that the distance between the photodetector and the cantilever is inconsequential to noise, as seen in Figure 8c. Therefore, angular noise can be minimized by 1) reducing the diameter of the collimated laser or by 2) increasing the focal length of the focusing lens.

Note, however, that it is the divergence of the *reflected* light that defines the noise – not the *incident* light. The following two subsections make use of this distinction, and propose two other methods for reducing the angular detection noise density.

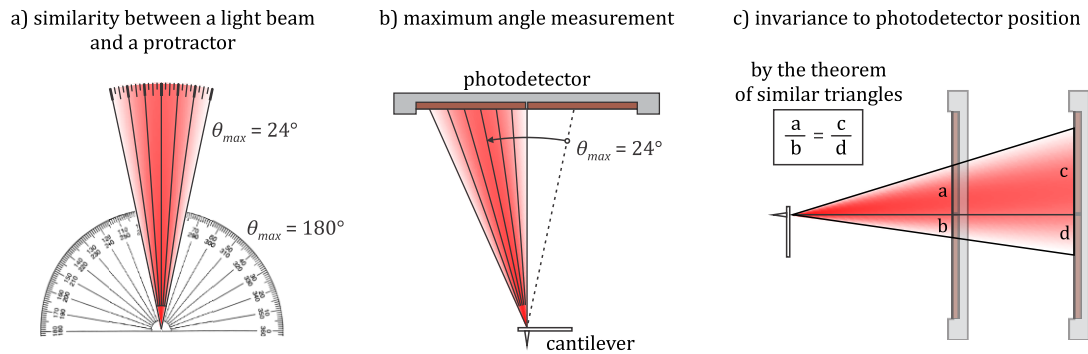


Figure 8: a) In AFM, a light beam is used as a protractor. b) The divergence angle determines the maximum measurable angle. c) The distance between the cantilever and the photodetector is inconsequential. (these illustrations only apply if the photodetector is in the far-field)

2.4.3 Exploiting cantilever curvature

The coating used to increase the reflectivity of cantilevers is known to cause stress-induced bending. This bending may prevent the light beam from reaching the photodetector if the cantilever is too curved. Consequently, Nanosensors™ cantilevers are guaranteed to have radii of curvature within an allowable “stress-free” tolerance of 6.6 mm (calculated from a tolerance of 3.5 % bending for a 450 μm -long cantilever, see

[Nanosensors](#).). Because such a cantilever is isotropically curved, it acts as a high-quality spherical mirror with a focal length of 3.3 mm. Note that this is $8\times$ stronger than the lens used to focus the light beam onto the cantilever! Nevertheless, the cantilever looks close to flat simply because of its small size, as seen in Figure 9a. This is merely an illusion.

Naturally, this cantilever cannot be treated as a plane mirror because it can strongly affect the divergence of the incoming light beam upon reflection. In fact, the divergence of a reflected light beam (50 μm diameter) can increase by up to 30% solely due to the cantilever curvature within the “stress-free” tolerance.

By moving the curved cantilever away from the light beam focus, the cantilever can be used as a powerful optical component: a collimator. If the focal length of a spherical mirror (the cantilever) matches the radius of curvature of the light beam wavefronts, the reflected beam is collimated, as illustrated in Figure 9c. Therefore, positioning the light beam focus ~ 3.3 mm above the curved cantilever results in a collimated reflected beam with a much lower divergence (assuming the focused light beam diameter < 50 μm). As long as most of the light is not lost due to the finite width of the cantilever, the angular detection noise drops significantly due to the lower divergence.

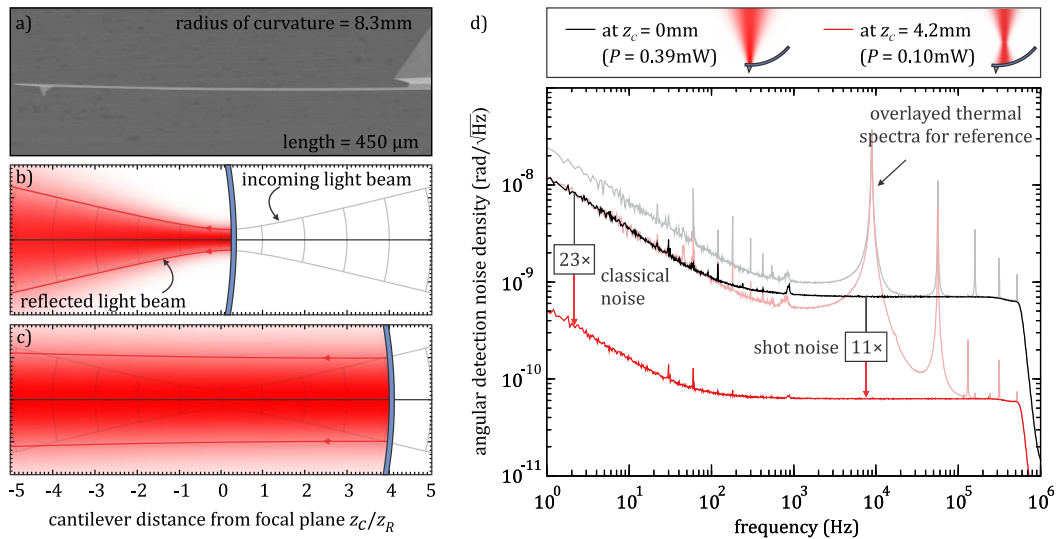


Figure 9: a) This cantilever is within the “stress-free” tolerance window set by Nanosensors™, yet its curvature is so strong that it acts as a perfect spherical mirror with focal length of 4.2mm. b) The divergence of a reflected focused light beam can increase, thereby increasing noise. c) Moving the cantilever away from the focus turns the cantilever into a collimator, thereby reducing the divergence and noise. d) The angular detection noise of a cantilever at the light beam focus, and away from the focus illustrates that noise can be reduced substantially using this method.

This idea was verified in Figure 9d, where the divergence was reduced by $23\times$, leading to a reduction in $1/f$ noise of $23\times$ and a reduction of shot noise by $11\times$ for a cantilever with a radius of 8.3 mm. The results, along with a more detailed derivation, were published in [4].

2.4.4 Fresnel-patterned cantilever coating

In 1823, Augustin Fresnel successfully manufactured his first multi-part lens, which is effectively a collapsed lens that maintains similar optical properties as a conventional lens. The goal was a significant reduction in weight and volume of the lenses used in lighthouses at the time.

A similar principle is used in this section to mimic a curved cantilever by patterning the coating of a flat cantilever. However, an alternative explanation will be provided for the noise reduction capabilities of the Fresnel cantilever shown in Figure 10.

Optical shot noise, in W/\sqrt{Hz} , grows proportionally to \sqrt{P} , implying that the optical power fluctuations increase with optical power P reaching the photodetector. On the other hand, the angular sensitivity of an OBD, in W/rad , increases linearly with the irradiance I_0 at the photodetector center. Therefore, the angular detection noise density, in rad/\sqrt{Hz} , is proportional to \sqrt{P}/I_0 – for shot noise – which can be decreased by minimizing the total optical power P while maximizing the irradiance I_0 . Figure 11 illustrates how the Fresnel cantilever achieves this seemingly-contradictory goal.

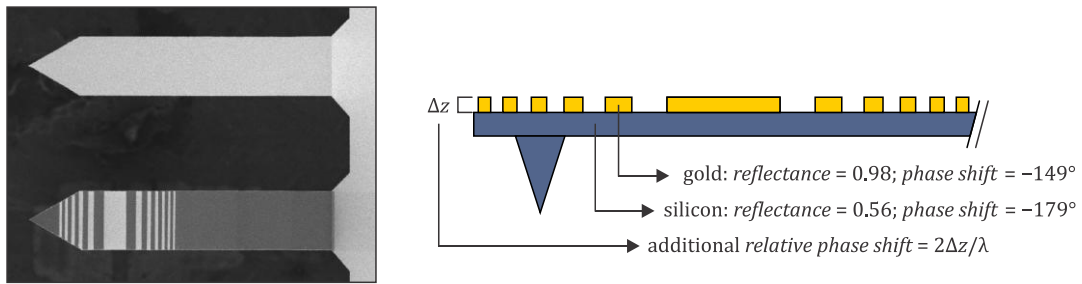


Figure 10: Fresnel cantilever (*below*) and regular gold-coated cantilever (*above*). The optical properties of the Fresnel cantilever are outlined (*right*). The pattern was fabricated by [field ion beam](#) (FIB) milling of a commercially gold coated cantilever ([Arrow™ TL2Au](#)).

Figure 11a depicts the typical situation where a light beam is focused onto a gold-coated cantilever, and reflected towards a photodetector. The irradiance distribution in the far-field $I_{FF}(\theta')$ is the squared-amplitude of the Fourier transform of the amplitude profile reflected off the cantilever $A_R(x)$, as explained by [Fraunhofer diffraction theory](#). Both profiles are Gaussian, and the divergence ϕ and the beam waist w_0 that define both of these distributions are locked by diffraction: $\phi = \lambda/\pi w_0$.

In Figure 11b, the cantilever is positioned at some distance z_c away from the light beam focus. Although the beam size w has increased such that $A_R(x|z_c)$ spans a wider area, the irradiance profile $I_{FF}(\theta')$ is identical to the previous situation. This invariance to z_c is attributed to the variable phase profile, which encodes the information that

defines the divergence of the beam. In other words, the Fourier transform of the complex-valued $A_R(x|z_c)$ is identical to the Fourier transform of the original $A_R(x)$. The benefits of having a larger reflected beam size during the Fourier integration of $A_R(x|z_c)$ are canceled by the fact that certain locations of $A_R(x|z_c)$ interfere destructively with each other. This suggests that there are locations along the cantilever where the reflected amplitude is reducing the irradiance I_0 .

Removing the gold-coating from locations which cause destructive light interference has a two-fold advantage: 1) reducing the noise by reducing the reflected light power P ; 2) increasing the signal by increasing the irradiance I_0 . This is illustrated in Figure 11c, where $I_{FF}(\theta')$ is far from Gaussian, but the two-fold advantage is achieved. Note that an additional benefit comes from the fact that the gold-coating has a finite thickness, such that any light reflected off the underlying silicon becomes closer in-phase with the light reflected off the gold.

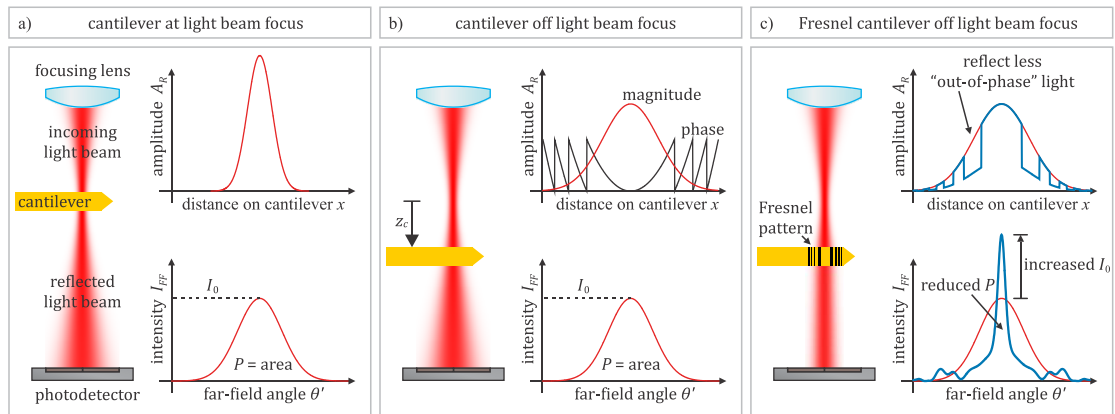


Figure 11: Demonstration, by three case studies, of how the Fresnel cantilever can increase the irradiance at the center of the photodetector I_0 while minimizing the total optical power P , both of which reduce the detection noise of cantilever deflection. Red curves relate to the gold-coated cantilever, whereas blue curves relate to the Fresnel cantilever.

Before proceeding, we mention an additional benefit of the Fresnel cantilever beyond the reduction of detection noise. As shown in Figure 9, there are true $1/f$ fluctuations of the cantilever that were made evident by the reduction of the detection noise (red curves). These measurable cantilever fluctuations are caused by coupling to the $1/f$ fluctuations of the light beam power via thermally stress-induced bending resulting from differences in the thermal coefficients of expansion of silicon versus gold. The added benefit of the Fresnel cantilever is the reduction of these true cantilever fluctuations by the stripping of the gold off the remainder of the cantilever body (beyond the Fresnel pattern) as seen in Figure 10.

3. Methodology

“The principle of science, the definition, almost, is the following: The test of all knowledge is experiment. Experiment is the sole judge of scientific “truth.””

– Richard Feynman

Scientific “truth” is usually described in terms of fundamental physical concepts such as force, mass, charge, etc., which we are all very familiar with. The data acquired by experiments, on the other hand, are usually records of voltage readings equidistant in time, such as acquired by analog-to-digital converters. Methodology is the study and development of the theoretical work which attempts to relate experimental data to true physical quantities. The goal of this section is to derive accurate theories and procedures for interpreting raw experimental data acquired by dynamic AFM.

The harmonic behaviour of an oscillating cantilever, in the point-mass approximation [46], can be described by three parameters: stiffness k , damping γ , and mass m . These parameters determine the transfer function of the cantilever $\mathcal{C}(\omega|k, \gamma, m)$. Consequently, these are the three *primary* physical properties that a cantilever can probe directly without additional calibration. In contrast, the measurement of any *secondary* physical property, such as force, temperature, distance, adhesion, roughness, viscosity, etc., requires additional calibration and/or theory.

Dynamic AFM can be operated using various control methods. Here, we discuss amplitude modulation (AM) AFM and frequency modulation (FM) AFM in detail. Once the Q -factor of the cantilever drops to ~ 1 and below, the advantages of driving on resonance vanish, and FM-AFM becomes unfeasible. In this thesis, AM-AFM is used for the overdamped cantilever in ionic liquid ($Q < 0.5$). However, FM-AFM still provides certain advantages over AM-AFM in underdamped environments, and is used for the hydration measurements in water, where $Q \sim 8$.

Both AM-AFM and FM-AFM experiments in this thesis require photothermal excitation - as an alternative to piezoacoustic excitation - to provide quantitative information about the tip-sample interaction, as will be described when contrasting both excitation methods in Sections 3.1.3 and 3.2.4.

3.1 Signal interpretation in AM-AFM

The cantilever transfer function $\mathcal{C}(\omega)$ has units of m/N, as it transduces a driving force amplitude F applied by the photothermal excitation system into a complex-valued oscillation amplitude Z . In AM-AFM, \mathcal{C} is measured with a lock-in amplifier, at a fixed frequency, by its magnitude response $|\mathcal{C}|$ and phase response θ_c , where $\mathcal{C} = |\mathcal{C}|e^{i\theta_c}$. These two measured parameters can be used to infer changes in stiffness and damping of the cantilever upon tip-sample perturbation. It is assumed that mass remains constant throughout the measurement.

3.1.1 Derivation of AM-AFM theory

Assuming that the cantilever can be described as a harmonic oscillator, the differential equation of motion relating its displacement $z(t)$ to the driving force $f(t)$ is

$$m\ddot{z} + \gamma\dot{z} + kz = f(t). \quad (7)$$

Taking the Fourier transform and solving for the reciprocal cantilever transfer function $\mathcal{C}^{-1} = F/Z$, herein referred to as the ‘‘cantilever impedance’’, results in

$$\mathcal{C}^{-1}(\omega) = [k - m\omega^2] + i\omega\gamma. \quad (8)$$

Unfortunately, the impedance \mathcal{C}^{-1} cannot be measured directly; rather, it is inferred from the measurement of \mathcal{C} as described earlier. Because m can safely be assumed constant, any change in stiffness is observed in the real component of \mathcal{C}^{-1} , as can be understood by inspection of Eq. (8). Similarly, any change in damping affects the imaginary component of \mathcal{C}^{-1} . This decomposition into real and imaginary components is represented in Figure 12a, which summarizes the AM-AFM derivation for the isolation of interaction stiffness and damping by [8]

$$\begin{aligned} k_i &= \frac{\cos\theta_c}{|\mathcal{C}|} - \frac{\cos\theta_{c_s}}{|\mathcal{C}_s|}, \\ \gamma_i &= -\frac{1}{\omega} \left[\frac{\sin\theta_c}{|\mathcal{C}|} - \frac{\sin\theta_{c_s}}{|\mathcal{C}_s|} \right], \end{aligned} \quad (9)$$

where the ‘‘s’’ subscript represents quantities measured at the start of the experiment, during calibration of the cantilever in the absence of tip-sample interactions. Note that mass plays no role in this AM-AFM derivation; its knowledge is only required for cantilever calibration, which is the topic of the next section.

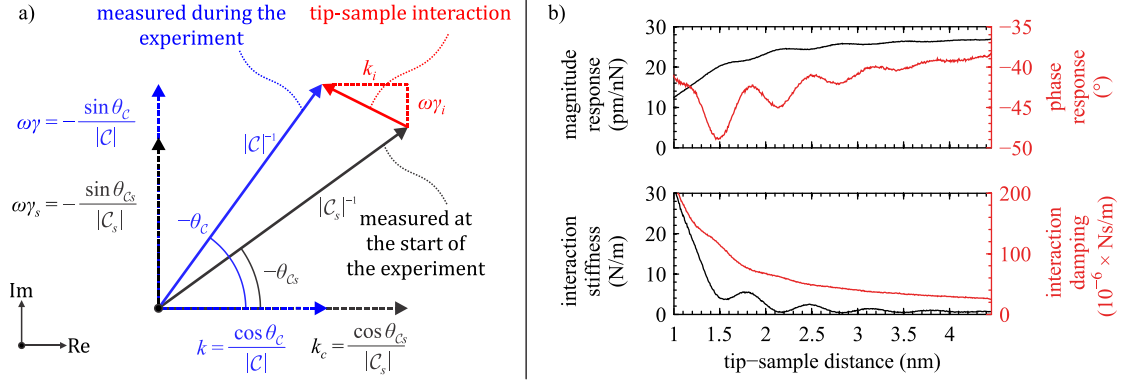


Figure 12: a) Derivation of AM-AFM theory for the extraction of interaction stiffness and damping. The real and imaginary components of \mathcal{C}^{-1} relate to conservative (k) and dissipative (γ) cantilever parameters, respectively. b) The theory is demonstrated on an approach curve in ionic liquid at a gold electrode. Note that both k and k_c are defined up to a constant ($m\omega^2$) that was omitted from this diagram for simplicity because only the difference $k_i = k - k_c$ is of interest.

3.1.2 Cantilever calibration in overdamped environments

As can be understood by inspection of Eq. (9), the cantilever must be calibrated at the start of the experiment to determine its starting phase θ_{Cs} and magnitude response $|\mathcal{C}_s|$. This step is imperative for accurately recovering the stiffness and damping profiles shown in Figure 12b. In overdamped environments, merely calibrating the cantilever becomes non-trivial, as the resonance peak disappears and the thermal noise barely hovers above the optical $1/f$ noise and shot noise. More problematically, the theory of cantilever hydrodynamics [44] predicts that the harmonic oscillator model breaks down as soon as $Q \sim 1$, and below, because damping γ and mass m effectively⁴ become frequency-dependent quantities. This frequency dependence violates the assumptions implicit to the harmonic oscillator model (Eq. (7)) and distorts the thermal spectrum of the cantilever. The cantilever can no longer be described by three parameters (k, γ, m).

However, an extended version of the theory of cantilever hydrodynamics [47] predicts additional squeeze-film damping for cantilevers near rigid walls. This is readily experimentally observable as a reduction in the Q -factor of up to $10 \times$ upon approaching the sample surface in highly viscous environments. More importantly, the extended hydrodynamic theory predicts that squeeze-film damping is frequency-independent, and therefore a single-valued γ can describe the damping of the cantilever. Furthermore, the remaining frequency-dependent mass m becomes negligible around and below the

⁴ The word “effectively” is used because the *actual* frequency dependence of m and γ does not necessarily change; rather, the relative bandwidth of the cantilever increases, thereby making this frequency dependence *effectively* much more observable and problematic.

resonance frequency of the cantilever, as $\omega\gamma \gg m\omega^2$, leading to the “massless model” of cantilever dynamics by simplification of Eq. (8) into [8]

$$\mathcal{C}^{-1}(\omega) = k + i\omega\gamma. \quad (10)$$

Note that this is simply the transfer function of a first-order low-pass filter. After calibrating the cantilever stiffness k in air, damping γ remains the only missing parameter to fully define \mathcal{C}^{-1} , and relates directly to the roll-off frequency ω_{ro} of the low-pass filter by $\gamma = k/\omega_{ro}$. This calibration procedure is summarized in Figure 13.

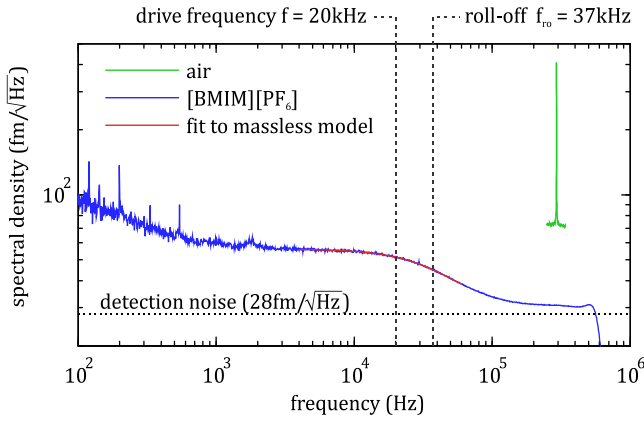


Figure 13: The thermal spectrum of the first eigenmode in air was used to calibrate the cantilever dynamic stiffness $k_c = 28.5$ N/m. The thermal spectrum in [BMIM][PF₆] was fit using the massless model to extract the roll-off for determining the damping by $\gamma = k/2\pi f_{ro}$. The endpoints of the fit were visually selected to avoid error caused by 1) $1/f$ noise at low frequencies and 2) thermal noise of higher eigenmodes at high frequency. Experiments are performed at the labelled drive frequency, in the middle of the fitting range.

After calibration, the cantilever magnitude and phase responses can be calculated at any frequency by

$$|C| = \frac{1}{k} \frac{1}{\sqrt{1 + (\omega/\omega_{ro})^2}}, \quad \text{and} \quad \theta_c = -\text{atan}\left(\frac{\omega}{\omega_{ro}}\right). \quad (11)$$

Furthermore, the accuracy of the massless model is strengthened by the fact that mass-loading due to squeeze-film effects actually decreases near solid surfaces at low [Reynolds numbers](#) (low frequency and high viscosity) [47]. This makes our initial assumption about a negligible mass even better than originally expected.

Finally, the deflection sensitivity, in units of nm/V, can be determined using the [fluctuation-dissipation theorem](#), which states that the thermal driving force is $F_T = 4k_B T \gamma_s$. The measured thermal spectrum becomes

$$F_T \times |C|^2 = \frac{4k_B T}{k_c \omega_{ro}} \frac{1}{1 + (\omega/\omega_{ro})^2} \quad (12)$$

This additional calibration step allows the measurement of secondary physical quantities, which can be inferred from the primary physical measurements of k and γ .

3.1.3 Limits to piezoacoustic excitation in AM-AFM

Piezoacoustic excitation relies on the Q -factor enhancement of the base movement: the tip oscillation amplitude $A = QA_b$, where A_b is the base amplitude. This relationship suggests that, in overdamped environments, the base of the cantilever moves with an amplitude *larger* than that of the tip. In this case, once the cantilever is pinned to the surface, the angular deflection of the cantilever becomes larger, even though the true tip amplitude is now zero [3]. The optical beam deflection method therefore sees a larger (apparent) oscillation amplitude. Imaging a surface with distance-feedback in this scenario requires the inversion of the feedback signal for stable imaging, because the amplitude *increases* upon approaching the sample.

Actually, the situation is much more complicated than described so far. In liquids, the cantilever can be excited by base movement *or* by acoustic excitation mediated by the liquid (in which case the base moves very little). The ratio between both channels of excitation is specific to the AFM hardware, frequency-dependent and time-varying. This renders the problem of imaging feedback unmanageable in overdamped environments.

Furthermore, the calibration of deflection sensitivity (nm/V) is frequency-dependent for low Q -factors due to the complexity of cantilever dynamics. It can differ by an order of magnitude from the expected value in a realistic setting of a viscous ionic liquid. This is shown in Figure 14, where recent modeling of piezoacoustic cantilever dynamics [43] were used, and compared to photothermal cantilever dynamics (assuming first eigenmode only).

In conclusion, piezoacoustic excitation in overdamped environments is not suitable for quantitative dynamic AFM, and unreliable even for simple topographical imaging.

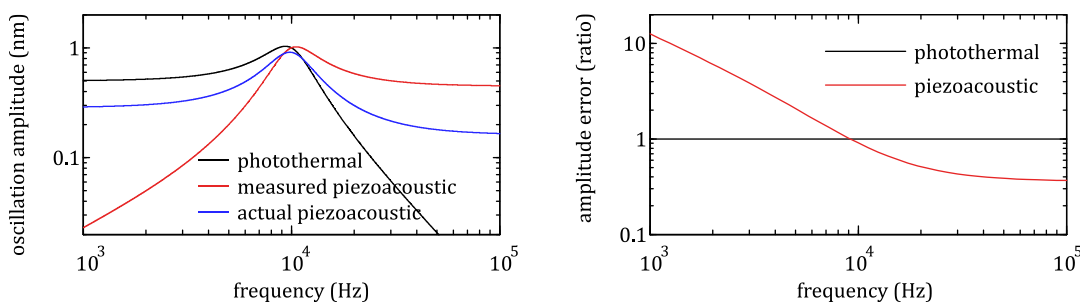


Figure 14: a) The first eigenmode of a driven cantilever with $Q = 2$ is simulated for photothermal excitation (with fixed force amplitude) and for piezoacoustic excitation (with fixed base amplitude) around the natural frequency (10 kHz). The photothermal response is simply that of a harmonic oscillator, i.e. the transfer function of the cantilever. As illustrated in (b), the amplitude measured by piezoacoustic excitation does not correspond to the actual oscillation amplitude, except near the resonance frequency. b) In other words, there is an amplitude calibration error when driving the cantilever off-resonance, which becomes inevitable for very low- Q environments.

FM-AFM differs from AM-AFM in that the cantilever is always driven at its natural resonance – in theory. The natural frequency ω_0 of the cantilever represents a special operating point where the parameters k and γ affect the phase and magnitude response of the cantilever transfer function, respectively. This condition is taken advantage of in FM-AFM, as ω_0 is actively tracked by positive feedback, thereby decoupling the measurements of conservative and dissipative forces.

The measured response of the cantilever is used as an excitation signal, with some added phase delay to promote self-excitation at ω_0 . Interestingly, thermal noise is sufficient for initiating this self-excitation process. The spontaneous oscillation occurs at the frequency for which the phase of the entire loop, including the cantilever phase θ_c , is an integer multiple of 2π . The frequency of the self-excited cantilever is measured throughout the experiment, and used as a measure of k .

The amplitude of excitation is controlled independently, to prevent the divergent behavior of positive feedback. The amplitude-controller is typically a proportional-integral feedback loop with an oscillation amplitude setpoint. It controls the amplitude of the excitation signal, described in the previous paragraph, to oppose any changes in cantilever magnitude response. This maintains the amplitude at the desired setpoint, and provides a measure of γ .

3.2.1 Derivation of ideal FM-AFM

Assuming that the cantilever can be described as a harmonic oscillator, the phase and magnitude components of its transfer function $\mathcal{C}(\omega|k, \gamma, m)$ are

$$\theta_c = \tan^{-1} \left\{ -\frac{\omega\gamma}{k - m\omega^2} \right\} \quad \text{and} \quad |\mathcal{C}| = -\frac{\sin \theta_c}{\omega\gamma}. \quad (13)$$

Conveniently, the sole condition for keeping the cantilever on resonance is $k = m\omega^2$. Therefore, by the [binomial approximation](#), any fractional change in frequency $\Delta\omega_0/\omega_0$ is equal to half the fractional change in stiffness $\Delta k/k_c$, such that

$$k_i = 2k_c \times \frac{\Delta\omega_0}{\omega_0}, \quad (14)$$

where $\Delta k = k_c + k_i$ was used, and k_c was assumed frequency-independent.

Note that the magnitude $|\mathcal{C}|$ is expressed in terms of (θ_c, γ) instead of the native parameters (k, m, γ) . This is a convenient reparameterization of the transfer function in the context of FM-AFM, because phase is locked by the self-excitation process. For a

constant phase, $|\mathcal{C}|^{-1} \propto \omega\gamma$. Because the drive amplitude Λ opposes changes in $|\mathcal{C}|$, it is proportional to ω and γ :

$$\Lambda = \frac{\omega\gamma}{\omega_s\gamma_s}, \quad (15)$$

where the “s” subscript represents quantities measured at the start of the experiment. Note that the dimensionless drive amplitude Λ has also been normalized at the start of the experiment, as only *relative* changes in the drive amplitude are physically relevant. Eq. (15) is trivial: in the context of viscous damping, it is easier to drive a cantilever at either a lower frequency or in a less viscous medium.

During an experiment, the damping γ changes for two reasons: 1) additional damping γ_i due to tip-sample interaction; 2) frequency dependence of damping γ_c of the cantilever itself: i.e. $\gamma = \gamma_i + \gamma_c(\omega)$. Isolating the parameter of interest in Eq. (15) returns

$$\gamma_i = \gamma_s \left(\Lambda \frac{\omega_s}{\omega} - \frac{\gamma_c}{\gamma_s} \right). \quad (16)$$

Changes in ω are measured experimentally, whereas variation in γ_c can be computed using Sader hydrodynamic theory [44]. Note that any changes in ω and $\gamma_c(\omega)$ caused by conservative forces result in $\gamma_i = 0$, as required.

3.2.2 *Transfer functions of the AFM system*

Because the frequency of excitation varies throughout an FM-AFM measurement, it is necessary to measure the transfer functions of the AFM system, and assess their impact on the measured signals. Figure 15 depicts a schematic of the FM-AFM system. The measured signals $(\Delta\omega, \Lambda)$ are separated from the desired signals $(\Delta\omega_0, \gamma_i)$ by the transfer functions of the excitation \mathcal{X} and detection \mathcal{D} systems. Note that the self-excitation frequency shift $\Delta\omega$ and the cantilever frequency shift $\Delta\omega_0$ are different quantities.

Using a network analyzer (Agilent 4395A), the driven response of the cantilever was measured. This results in the combined transfer function \mathcal{XCD} , as can be understood from Figure 15. The transfer function of the excitation system \mathcal{X} can be isolated by independently measuring the transfer function of the detection system \mathcal{D} , and the transfer function of the cantilever \mathcal{C} . The transfer function \mathcal{D} was independently measured with the network analyzer (not shown), while \mathcal{C} was deduced by fitting its thermal power spectrum with a harmonic oscillator model. Using the simple harmonic oscillator model here is warranted by the fact that the Q -factor was high (~ 8). The transfer function of the phase shifter was verified to be flat. This completes the characterization of the AFM, as summarized in Figure 16.

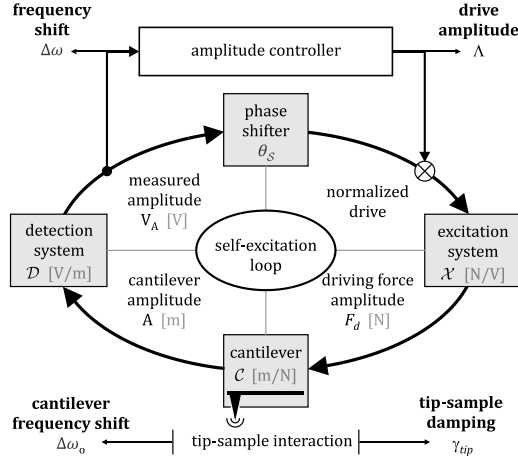


Figure 15: System diagram of an FM-AFM system, where self-excitation is achieved by driving the cantilever by its own measured deflection signal. The grey boxes represent transfer functions that make up the self-excitation loop.

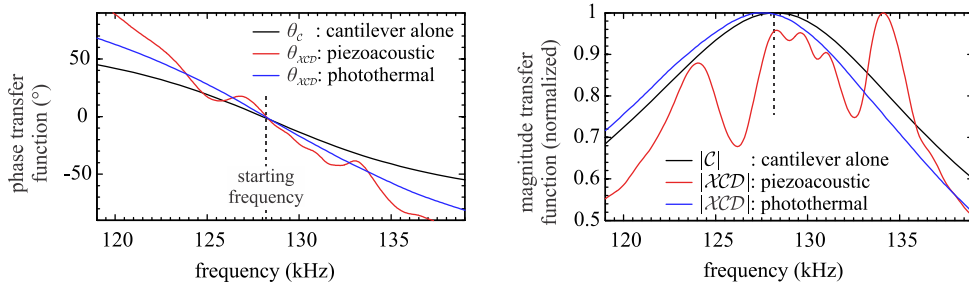


Figure 16: Phase and magnitude transfer functions of the cantilever alone (ideal FM-AFM), and including the detection and excitation systems (real FM-AFM) for photothermal and piezoacoustic excitation.

A modest deviation from ideal behaviour is observed in the case of photothermal excitation. The deviation is well defined, and stationary in time, such that recovery of the stiffness and damping can be performed accurately, as described in the following section.

The deviation from ideality caused by the piezoacoustic excitation system is stark. Its effects on the FM-AFM measurements will be discussed in Section 3.2.4.

3.2.3 Derivation of real FM-AFM in liquid environments

This section includes the AFM system transfer functions to the FM-AFM derivation. Rather than repeating tedious mathematical derivations, results will be adopted from [6] and explained heuristically here.

The slope of the cantilever phase spectrum β_c differs from that of the entire excitation loop $\beta_{x_{CD}}$, as clearly observable in Figure 16 (the convention $\beta = \partial\theta/\partial f$ is adopted herein). For photothermal excitation, the added slope $\beta_{x_{D}}$ is constant around the resonance across the measured frequency range. As derived by Kobayashi et al. [48], the cantilever frequency shift $\Delta\omega_o$ can be calculated from the measured frequency shift $\Delta\omega$ by

$$\Delta\omega_o = \frac{\beta_{x_{D}} + \beta_c}{\beta_c} \Delta\omega. \quad (17)$$

This relationship can be illustrated by a simple scenario. Say $\beta_{x_{D}} = \beta_c$, and the cantilever shifts by $\Delta\omega_o = 1$ kHz. In that case, the self-excitation loop will shift only by $\Delta\omega = 0.5$ kHz because any phase shift in the AFM system $\Delta\theta_{x_{D}}$ is compensated by an opposite phase shift in the cantilever $\Delta\theta_c$; the oscillation frequency for which the total $\theta_{x_{CD}}$ remains fixed is therefore midway between the starting frequency and the new cantilever resonance frequency. This correction factor was applied in Figure 17 to extract an accurate force profile measured at the mica/water interface.

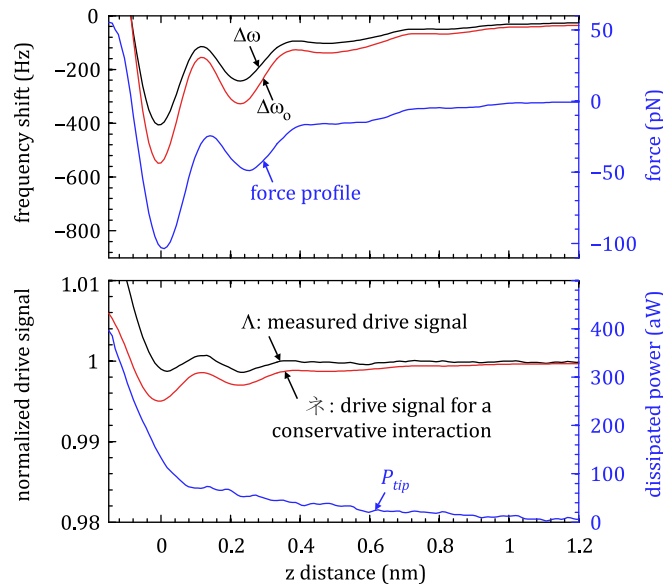


Figure 17: These approach curves in water on mica were acquired after the AFM system characterization in Figure 16. Eq. (17) was used to obtain the cantilever frequency shift $\Delta\omega_o$ from the measured frequency shift $\Delta\omega$. Then, a force deconvolution method was used to transform $\Delta\omega_o$ into a force profile [49]. Eq. (19) was used here to calibrate the drive signal into a damping, and then a dissipated power.

The phase shift of the cantilever described above will have an effect on the drive amplitude Λ , as driving a cantilever off-resonance is less efficient. The driving efficiency is proportional to $\sin\theta_c$, as can be understood from Eq. (13). Furthermore, if the magnitude of the excitation $|\mathcal{X}|$ decreases due to a frequency shift, the drive amplitude Λ

will increase proportionally to maintain the cantilever oscillation amplitude constant. Lastly, if the magnitude of the detection $|\mathcal{D}|$ decreases, the amplitude-controller will increase the drive amplitude to compensate for the *apparent* decrease in oscillation amplitude. These three scenarios imply that the drive amplitude Λ is frequency dependent due to instrumental transfer functions. In other words, the drive amplitude is expected to change in a purely conservative interaction.

Let the dimensionless calibration factor $\ddagger(\omega)$ represent the frequency dependence of the drive amplitude:

$$\ddagger(\omega) = \left| \frac{\sin(\theta_{c_s} - \Delta\theta_{x\mathcal{D}})}{\sin(\theta_{c_s})} \right|^{-1} \left| \frac{\mathcal{X}}{\mathcal{X}_s} \right|^{-1} \left| \frac{\mathcal{D}}{\mathcal{D}_s} \right|^{-1} \left(\frac{\omega}{\omega_s} \right). \quad (18)$$

The first three factors were explained in the previous paragraph, while the ω factor (caused by viscous damping) was adopted from the ideal FM-AFM derivation (Eq. (16)).

Before proceeding with the extraction of damping from Λ , any expected change due to frequency dependence should be divided out as in $\Lambda/\ddagger(\omega)$. This calibration procedure corrects the ideal FM-AFM derivation into [6]

$$\gamma_i = \gamma_s \left(\frac{\Lambda}{\ddagger} - \frac{\gamma_c}{\gamma_s} \right). \quad (19)$$

Using the measurements of $\theta_{x\mathcal{D}}$ and $\mathcal{X}\mathcal{D}$ presented in Figure 16, the damping profile at the water/mica interface was recovered in Figure 17. The oscillations in the drive signal are caused only due to the frequency dependence of viscous damping and of the AFM system, whereas the recovered damping γ_i is monotonic.

Ongoing controversies within the scientific community relate to the debate between oscillatory versus monotonic damping of confined fluids [40,41,50]. Omitting any of the correction factors in Eq. (18) and (19) causes an oscillatory damping component to appear above noise in Figure 17, thereby stressing the necessity for using this new FM-AFM theory for the recovery of damping from the drive signal. We believe that the root of many scientific disagreements about a monotonic vs oscillatory damping profiles are rooted in improper instrumental characterization and invalid approximations used to derive AFM theory.

3.2.4 *Limits to piezoacoustic excitation in FM-AFM*

The recovery of damping for data similar to that in Figure 17, but acquired by piezoacoustic excitation, is practically impossible. This, however, is not a shortcoming of the theory used to recover damping, nor is it due to poor experimental practice in

measuring the piezoacoustic transfer function \mathcal{X} . The temperature-dependence of the acoustic velocity of water (0.2 %/°C) causes the \mathcal{X} to change with time, as is well-known and observable on any liquid AFM. Hence, 40 mK of drift is expected to cause a 10 Hz shift in any resonance peak of the liquid cell near 130 kHz. Figure 18 demonstrates the expected effects of 10 Hz shift on a) the measurement of $|\mathcal{X}|$ which is barely noticeable, b) the resulting measured drive amplitude signal which is nearly unaffected, and c) the recovered damping.

In summary, 40 mK of unaccounted temperature drift prevents the recovery of an accurate damping profile in our experiment, if piezoacoustic excitation is used [6]. The strong dependence between the measurement of $|\mathcal{X}|$ and the recovered damping is caused by the fact that $\sim 99\%$ of the drive amplitude drives the cantilever damping, while only $\sim 1\%$ drives the interaction damping. Therefore, a small change in the total drive amplitude can be misinterpreted as a large change in interaction damping if $|\mathcal{X}|$ is neglected. This can change a true monotonic damping signal into an apparent oscillatory one, as was demonstrated in Figure 18.

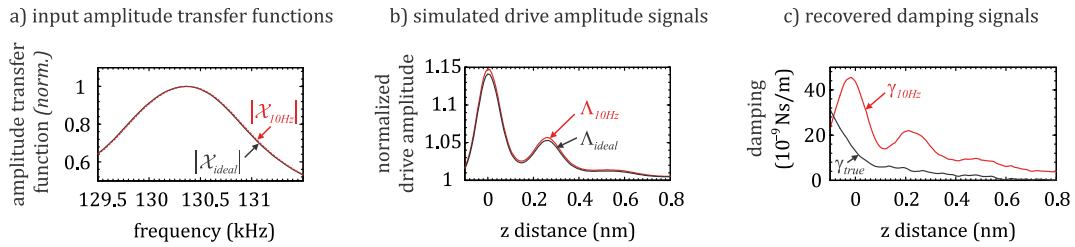


Figure 18: The black simulated measurements represent the ideal situation with no drift. The red measurements assume that 40 mK of drift occurred between the measurement of $|\mathcal{X}|$ and the force spectroscopy experiment.

3.3 Stochastic simulation of hydration measurements

In this section, a hydration measurement of water on mica is simulated to assess the impact of detection noise, force noise, and displacement noise, which were introduced in Section 2.3. Any noise source can be classified into one of these categories depending on how it affects the outcome of an AFM experiment and where it enters an AFM simulation. Although detection shot noise and thermal force noise set the fundamental limit of sensitive nanoscale experiments, displacement noise due to external mechanical vibrations, as described in Section 2.1, can dominate the measurement, as will be shown.

3.3.1 AFM characterization

The following simulation is performed using a 30 μm long 15 μm wide silicon cantilever with a stiffness $k = 10 \text{ N/m}$. This cantilever was modelled using Sader hydrodynamics [44] for the first eigenmode in water. The frequency-dependent mass $m(\omega)$ and damping $\gamma(\omega)$ were computed from the Sader hydrodynamic function to determine the cantilever impedance

$$C^{-1}(\omega) = k - m(\omega)\omega^2 + i\omega\gamma(\omega). \quad (20)$$

The natural frequency $\omega_0 = 350 \text{ kHz}$ and $Q \sim 6$.

The three spectral densities plotted in Figure 19a characterize the noise of the AFM according to our noise characterization established in Section 2.3. These noises were used as input for the hydration experiment simulation; they were measured/modelled as follows.

The force noise n_{force}^2 relates to $\gamma(\omega)$ by the fluctuation-dissipation theorem [51]:

$$n_{force}^2 = 4k_B T \times \gamma(\omega). \quad (21)$$

This noise scales as $n_{force}^2 \sim \omega^{0.52}$ and reaches $1.3 \times 10^{-26} \text{ N}^2 \text{ Hz}^{-1}$ at ω_0 . The exponent of this power law was determined by fitting the numerically defined Sader model around ω_0 . The cantilever deflection noise density in the absence of tip-sample interactions is given by $n_{force}^2 \times |C|^2$, which was plotted in Figure 19a.

The angular detection noise density of our optical beam deflection system was measured to $5 \times 10^{-19} \text{ rad}^2 \text{ Hz}^{-1}$ at high frequencies [4], corresponding to an expected $15^2 \text{ fm}^2 \text{ Hz}^{-1}$ of detection noise n_{detect}^2 for a 30 μm long cantilever.

The displacement noise was empirically measured on our home-built AFM by pressing a cantilever against a flat sapphire surface, acquiring a power spectral density, and then subtracting the detection noise to obtain n_{disp}^2 . A passive vibration isolation table was used. The displacement noise integrates to 36 pm across a [1 Hz, 10 kHz] bandwidth. This measurement compares well with high-end AFMs: our number falls in between the vibrations of the [Dimension Icon](#) and [Dimension FastScan](#) AFMs (Bruker, Santa Barbara, CA), specified by the manufacturer as 30 pm and 40 pm, respectively, for a bandwidth up to 625 Hz. Our measurement also falls very close to the 35 pm specified for the [NanoWizard 3 Nanoscience](#) AFM (JPK, Berlin) across a [1 Hz, 1 kHz] bandwidth. This makes the following simulation quantitatively relevant to the majority of AFM users.

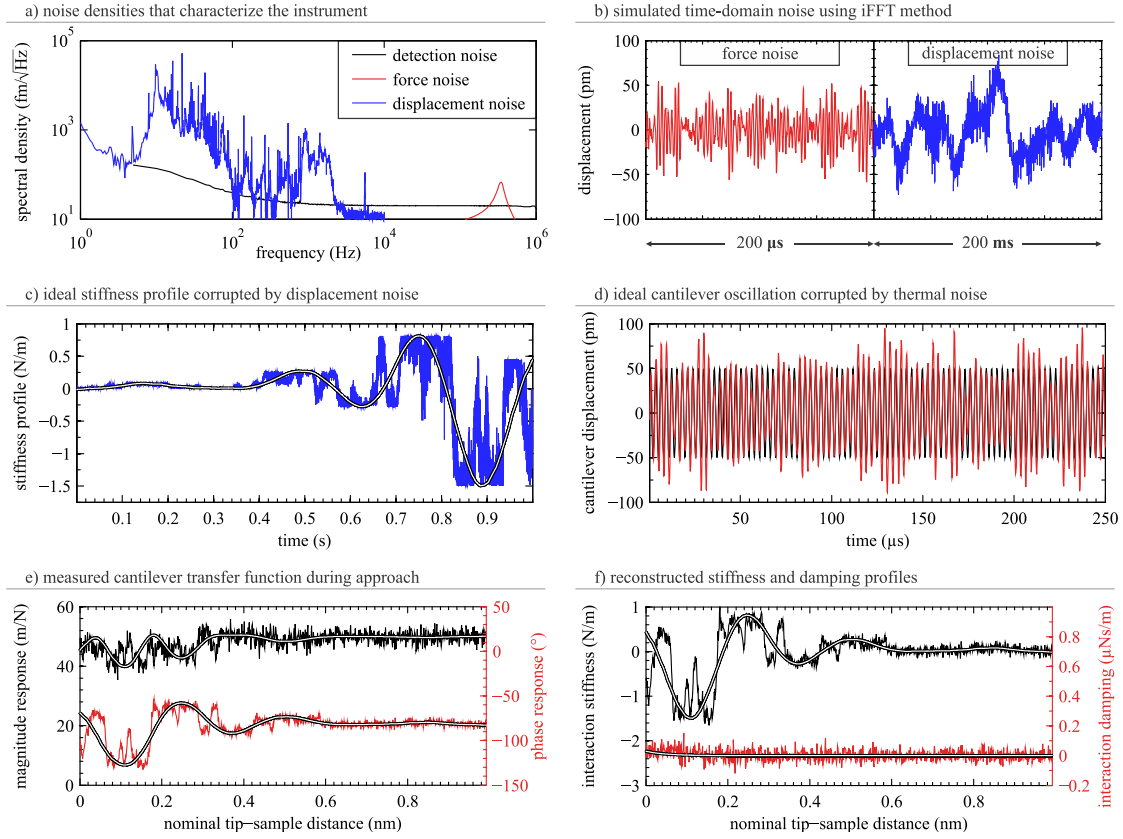


Figure 19: Outline of the simulated hydration experiment. The spectral densities in (a) were used to simulate time-domain data (b). Displacement noise causes an imperfect stiffness profile seen by the cantilever tip (c), and the force noise adds to the driven cantilever oscillations (d). Detection noise has no measurable impact on the outcome of this experiment. The magnitude and phase response of the cantilever was measured (e), and used to extract the stiffness and damping profiles (f). White lines in (c-e-f) relate to ideal (noiseless) measurements.

3.3.2 AFM simulation

In a recent article [15], we described the statistics of the power spectral density (PSD) in the context of noise in AFM, and described the “iFFT method” for generating time-domain stochastic noise directly from a numerically-defined PSD of stationary noise. The iFFT method was used to simulate time-domain noise vectors ϵ_{force} , ϵ_{detect} , ϵ_{disp} from their corresponding PSDs n_{force}^2 , n_{detect}^2 , n_{disp}^2 . These vectors were generated for a duration of 1 sec, and the sampling rate was set to 10 MHz to fully resolve the cantilever oscillations. Portions of the simulated ϵ_{force} and ϵ_{disp} are plotted in Figure 19b, whereas detection noise was not plotted for simplicity.

The aforementioned simulated cantilever was approached towards the mica surface in water at a rate of $v = 1$ nm/s. During the simulated approach, the tip was subject to an oscillatory stiffness profile. The interaction stiffness $k_i(h)$ and damping $\gamma_i(h)$ profiles

from Figure 17 were used as input for this simulation, where h is the tip-sample distance. The interaction impedance

$$J^{-1}(h) = k_i(h) + i\omega\gamma_i(h) \quad (22)$$

adds to \mathcal{C}^{-1} from Eq. (20), resulting in the perturbed cantilever impedance $\mathcal{C}_i^{-1}(h) = \mathcal{C}^{-1} + J^{-1}(h)$.

Importantly, the displacement noise causes dithering of the stiffness and damping profiles acting on the cantilever tip. Instead of a perfectly linear approach in time, the tip-sample distance h changes as the sum of a linear function and the simulated displacement noise:

$$h(t) = vt + \epsilon_{disp}. \quad (23)$$

Reparametrizing $J^{-1}(h)$ as a function of time takes into account mechanical vibrations, as shown in Figure 19c.

During the approach, the time-varying $\mathcal{C}_i^{-1}(t)$ was inferred by driving the cantilever on resonance with a sinusoidal force, which is inevitably corrupted by force noise,

$$f(t) = F_d e^{i\omega_0 t} + \epsilon_{force}, \quad (24)$$

and measuring the cantilever deflection $z(t)$, which is corrupted by detection noise,

$$z(t) = \mathcal{C}_i(t) \times f(t) + \epsilon_{detect}. \quad (25)$$

The driving force amplitude $F_d = 200$ pN resulted in an oscillation amplitude of 50 pm prior to tip-sample interaction. Furthermore, because the damping remained nearly constant during this measurement ($\gamma_i \ll \gamma$), the thermal force noise was accurately approximated as stationary throughout the experiment, thereby validating the iFFT approach used to generate ϵ_{force} earlier.

Next, the magnitude response $|\mathcal{C}_i|$ and phase response $\theta_{\mathcal{C}_i}$ of the perturbed cantilever was calculated by demodulating the deflection signal $z(t)$ with respect to the driving force $f(t)$. The demodulation bandwidth of 1 kHz, resulted in 1000 data points for the 1 sec approach curve. The cantilever displacement signal was filtered using a 4th order Butterworth filter with cutoff frequency of 500 Hz. The results are shown in Figure 19e.

Finally, both magnitude and phase signals were used to extract estimates of the interaction stiffness k_i and damping γ_i using AM-AFM theory described by Eq. (9). The resulting k_i and γ_i are plotted in Figure 19f, where any deviations from the ideal profiles are attributable to noise.

Detection noise contributes to $< 3\%$ of the variability of the measured cantilever displacement in this simulated experiment, making its impact on the extraction of k_i and γ_i negligible. This statement remains true irrespective of the cantilever oscillation amplitude, and is valid for demodulation bandwidths up to corner frequency of the cantilever ($f_0/2Q = 9$ kHz).

Far from the surface, force noise dominates the signal variability. As can be understood from Eq. (21), damping (γ) is the only free parameter for reducing the thermal force noise of a room-temperature AFM experiment. It is well established that damping scales with the physical size of cantilevers [52,53]. This is why a small cantilever was chosen for this simulated experiment.

Close to the surface, displacement noise overshadows the effects of thermal noise on the measurement of the stiffness profile. Unlike thermal noise, the tip-sample vibrations have a spectral signature that is far from white. This occurs because the bulk of the displacement noise falls below the demodulation bandwidth of 1 kHz. AFM mechanical vibrations are slow, even on the timescale of the 1 sec approach. On the other hand, the damping measurement remains limited by thermal noise.

In summary, these observations imply that the fundamental limits set by optical shot noise (detection noise) and cantilever thermal noise (force noise) are dominated by mechanical vibrations (displacement noise) for the *stiffness* measurements of the last two hydration layers in our experiment, while thermal noise completely overwhelms the *damping* signal.

Turning on the active vibration isolation of our [TS-150](#) (Herzan, Languna Hills) reduces most of these low-frequency vibrations, and lowers the displacement noise to within a 12-18 pm range on our AFM. This results in a much more faithful measurement of the hydration profile (see SI). Even better performance is expected from a [Cypher](#) AFM (Asylum Research, Santa Barbara, CA), which is specified to < 15 pm displacement noise across the [0.1 Hz, 1 kHz] bandwidth, and < 5 pm in quiet environments. Only an AFM with such low displacement noise can take full advantage of the thermal noise reduction offered by small cantilevers.

4. Hydration structures of water on mica

[Surface force apparatus](#) (SFA) studies, performed in equilibrium conditions, suggest that the fluidity of water remains high near solids because of the suppression of hydrogen bond networks related to its solid-like behavior, whereas organic solvents see an increase in viscosity near solid interfaces due to the reduction in translation degrees of freedom [21]. Recent AFM research extended this picture by suggesting that solid-like behavior of water can arise in certain dynamical conditions [54]. Both of these studies probe large contact areas, and therefore relate to the mesoscopic properties of water *films*. Here, AFM is used to measure the distribution of water *molecules* on an atomic length-scale via direct force imaging by employing sharp tips. The results are relevant for direct comparison to molecular dynamic simulations, with the goal of extending our knowledge about water at the nanoscopic scale. Such experiments are crucial for understanding the role of water in biomolecular interactions, for example, which involve a small number of water molecules.

In the first subsection, the electric double layer theory is derived to understand the distribution of charge carriers in aqueous solutions near solid interfaces. Then, atomic-resolution hydration force spectroscopy is carefully analyzed using the new FM-AFM theory derived in Section 3.2.3 to extract physically accurate tip-sample interactions. The damping signal is correlated to the tip-sample distance and discussed with reference to simulations. The section closes with a discussion about the ongoing oscillatory versus monotonic damping debate.

4.1 The electrical double layer

Understanding the electric double layer theory, and all of its underlying assumptions, is key for critical interpretation of observations at the solid-liquid interface (SLI). Whether the surface is conductive or not, electrochemical phenomena influence the behavior of charge concentration profiles in the liquid.

In 1853, Helmholtz discovered that the SLI acts like a double-plate capacitor. Opposite charge carriers meet at the SLI, separated by the charge carrier radius r . This linear model predicts a constant areal capacitance $C = \epsilon/r$, in units of F/m^2 , where ϵ is the permittivity of water.

In the 1910s, Gouy and Chapman imagined the SLI as composed of diffusive non-interacting infinitely-small charge carriers subject to a hard boundary condition. Every charge on the solid draws an opposite charge in the liquid towards the surface. The

average distance between both charges is determined by thermal fluctuations (diffusivity) of the ions.

This model is widely used until today due to its mathematical simplicity. In fact, it represents the theoretical foundation of the Debye model for the EDL. Although its derivation is common to all electrochemical textbooks, it is worth solving from first principles to reexamine its assumptions and limitations. Also, it is used as a stepping stone for the derivation of ionic liquid EC theory presented in Section 5.

4.1.1 Statistical mechanics of the EDL

Luckily, the derivation and basic understanding of the EDL requires no knowledge of chemistry; it is simply an electrostatics problem with charge carriers subject to thermal fluctuations. The following model assumes non-interacting ions with no specific adsorption to the surface.

The one-dimensional [Poisson equation](#) can be used to solve for the charge distribution $\rho(x)$ in such a system:

$$\frac{d^2\psi(x)}{dx^2} = -\frac{\rho(x)}{\varepsilon}. \quad (26)$$

where $\psi(x)$ is the potential distribution. The charge distribution is composed of negative and positive ions: $\rho(x) = \rho_+(x) + \rho_-(x)$. Because charges are assumed to be non-interacting, they are only subject to [Boltzmann statistics](#). The probability of finding a charge at a distance x away from the surface is a function of $\psi(x)$:

$$\rho(x) = \rho_-(x) + \rho_+(x) = \rho_0 \cdot e^{\frac{\psi(x)}{\psi_T}} - \rho_0 \cdot e^{-\frac{\psi(x)}{\psi_T}}, \quad (27)$$

where ρ_0 is the charge of the solid surface, at $x = 0$, and the thermal potential $\psi_T = 25.7$ mV (at 300 K) represents the energy per unit charge caused by thermal fluctuations ($k_B T/e$).

Combining Eq. (26) and (27) results in the [Poisson-Boltzmann differential equation](#):

$$\frac{d^2\psi(x)}{dx^2} = -\frac{2\rho_0 \cdot \sinh\left(\frac{\psi(x)}{\psi_T}\right)}{\varepsilon}, \quad (28)$$

where $\tilde{\psi} = \psi/\psi_T$ is the dimensionless potential, in units of thermal potential.

Assuming ε is constant leads to the following solution:

$$\tilde{\psi}(x) = 2 \cosh^{-1} \left(\frac{e^{\tilde{\psi}_0} + 1 + 2e^{\tilde{\psi}_0/2} + (e^{\tilde{\psi}_0} + 1 - 2e^{\tilde{\psi}_0/2})e^{-2x/\lambda_D}}{e^{\tilde{\psi}_0} + 1 + 2e^{\tilde{\psi}_0/2} - (e^{\tilde{\psi}_0} + 1 - 2e^{\tilde{\psi}_0/2})e^{-2x/\lambda_D}} \right) \quad (29)$$

where the [Debye length](#) $\lambda_D = \sqrt{\frac{\epsilon\psi_T}{2\rho_0}}$ (for monovalent species). For example, the Debye length of a 0.25 M KCl is [0.43 nm](#), whereas it is almost 1 μm in distilled water.

As long as thermal fluctuations dominate over electric fields, i.e. $\tilde{\psi} < 1$, the above potential distribution can be approximated as exponential:

$$\psi_D(x) = 2\psi_0 \cdot e^{-\frac{x}{\lambda_D}}, \quad (30)$$

where ψ_0 is the surface potential, at $x = 0$. This is known as the [Debye-Huckel approximation](#) in the linear electrochemical (EC) regime, where both the potential $\psi(x)$ and charge $\rho(x)$ distributions are exponential with a decay length λ_D . The capacitance in this regime is constant, and determined by $C_D = \epsilon/\lambda_D$.

When the surface potential exceeds the thermal potential (25.7 mV), the system falls into the weakly nonlinear EC regime and both the potential and charge distributions deviate from exponential. This occurs because electrostatic attractions exceeds thermal fluctuations. Eq. (29) provides the functional form of the potential, which is plotted in Figure 20. The Debye length loses its original significance; the actual screening length decreases because charge-carriers crowd around the SLI. Consequently, the differential capacitance increases (exponentially) with surface potential $\tilde{\psi}$:

$$C_{GC}(\tilde{\psi}) = C_D \cdot \cosh \tilde{\psi}. \quad (31)$$

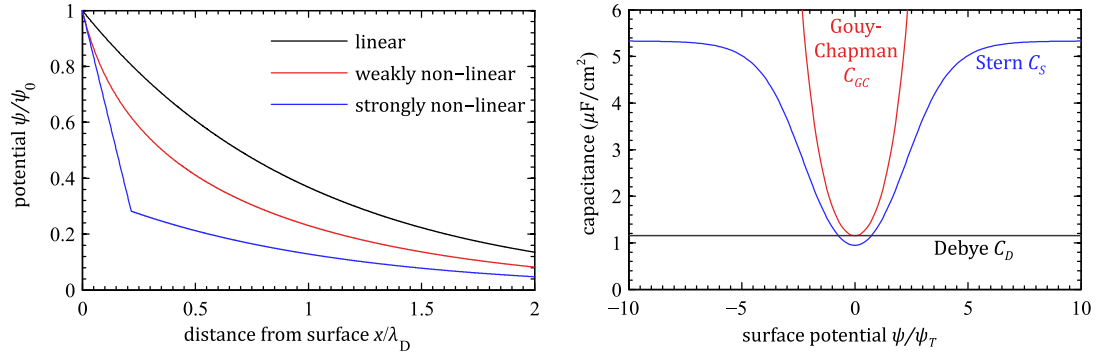


Figure 20: Potential distribution for the three EC regimes. Differential capacitance for the Debye, Gouy-Chapman approximations and Stern correction.

Increasing the surface potential further causes the electrolyte concentration at the interface to saturate. This is termed the steric limit potential, which marks the start of the strongly nonlinear EC regime. Due to the exponential dependence of Boltzmann statistics, the steric limit potential is surprisingly low. For example, a solution with a bulk molarity of 10^{-5} M will have a 5 M concentration at the SLI for an applied potential of only 330 mV ($\sim 13 \psi_T$). For concentrated electrolytes, this regime may begin at potentials as low as a few ψ_T .

Around and beyond the steric limit, the solution to the Poisson-Boltzmann equation breaks down as the predicted ionic concentrations near the SLI become unphysically large. The diverging concentration is a result of the “infinitely-small charge carrier assumption”. In 1924, Stern suggested a correction factor for this problem by recalling Helmholtz’ original idea of a double-plate capacitor. Adding the Helmholtz capacitance C_H in series results in the Stern capacitance

$$C_S^{-1} = C_{GC}^{-1} + C_H^{-1}, \quad (32)$$

The resulting potential $\psi(x)$ and capacitance C_S are plotted in Figure 20.

4.2 Atomic-resolution hydration experiment

4.2.1 Three-dimensional force spectroscopy

The three-dimensional hydration map in Figure 21 was acquired in aqueous 0.25 M KCl on muscovite mica, using FM-AFM on a modified Shimadzu AFM with home-built self-excitation electronics and retrofit with photothermal excitation.

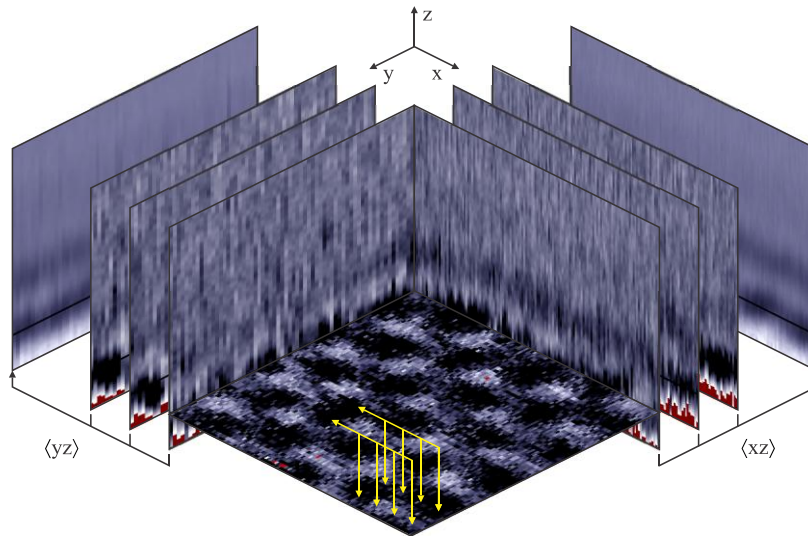


Figure 21: 3D frequency shift map in 0.25 M KCl at the mica interface, which is a measure of the water density distribution above the mica surface with features in the lateral and perpendicular direction to the surface. The acquisition process is illustrated by the yellow arrows. This dataset is composed of 8320 force spectroscopy profiles in the z direction, taken on an xy grid. A threshold frequency shift limits the extent of each approach distance: once the threshold is exceeded upon approaching, the tip is retracted and the process is repeated at the next (x,y) position. This results in a partially filled 3D matrix; red pixels represent pixels that contain no data. The cantilever (PPP-NCH, NanoSensors) had a natural frequency of 128.8 kHz, a stiffness of 23.7 N/m, and a quality factor of 7.7. Dimensions in pixels: $128 \times 65 \times 119$. Nominal dimensions in nm: $2.2 \times 1.7 \times 1.1$. Amplitude set point: 0.33 nm peak-to-peak. The average frequency shift profile of this dataset was presented in Figure 17. A [movie online](#) displays several xy , yz , and xy slices of this dataset.

All 128×65 approach curves from the hydration map of Figure 21 were averaged, and processed by the new FM-AFM theory presented in Section 3.2.3. The results are plotted in Figure 17.

4.2.2 *Nanoscopic vs mesoscopic hydration experiments*

An important piece of information remains unknown - the tip shape. However, the atomic-scale lateral resolution seen in the inset of Figure 21 suggests that the interaction force is dominated by no more than a few atoms. Such a small tip apex results in small dissipative losses. The recovered dissipated power on the order of 100 aW corresponds to a damping of $\sim 10^{-8}$ Ns/m, which is five orders of magnitude smaller than observed in a recent study of the dynamic solidification of confined water films [54] performed with a ~ 100 nm tip radius. Before proceeding, these two types of AFM experiments should be clearly distinguished; they are illustrated in Figure 22.

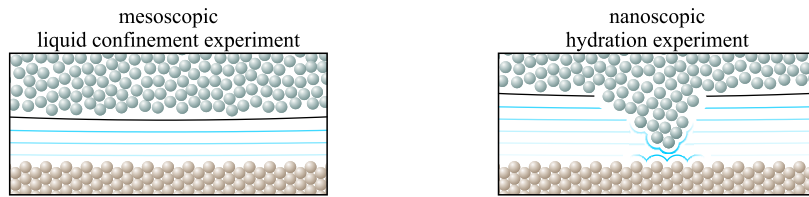


Figure 22: In a mesoscopic liquid confinement experiment, continuum fluid dynamics are used to model the rheological properties of a water film confined between a tip (upper) and a surface (lower). The tip is characterized by its radius. In a nanoscopic hydration experiment, the stochastic behavior of individual water molecules around the tip apex must be taken into consideration. Nevertheless, the overhanging mesoscopic tip can affect the acquired data, and should be taken into consideration when interpreting nanoscopic hydration data.

Mesoscopic liquid confinement experiments study the rheological properties of water *films* trapped in between a blunt tip and a flat sample, using the framework of continuum hydrodynamics. At distances below 2 nm, oscillatory forces are observed as they “rupture” individual water layers by displacing thousands of water molecules in unison. Such a thermodynamically irreversible process costs a large amount of energy and leads to large oscillatory damping and solid-like behaviour in certain dynamical conditions that strongly depend on the shear rates [54], surface roughness [55], etc.

In a nanoscopic hydration experiment, the tip-sample interaction involves a countable number of water molecules, whose dynamics and steric arrangements around single atoms are being probed. Sharp tip geometries allow the study of site-specific force profiles above atomically resolved surface atoms, as shown recently by Fukuma *et al.* [22] and Kobayashi *et al.* [56]. In this work, we extend their site-specific force

spectroscopy investigations by analyzing the damping information made possible by the photothermal excitation used to excite the cantilever. Our results provide complementary information to strengthen the understanding of dynamical properties of water molecules in different hydration layers.

4.2.3 Damping in nanoscopic hydration experiment

While our tip apex moves at around $100 \mu\text{m/s}$ with an oscillation period of $8\mu\text{s}$, water molecules move at an average speed of 600 m/s , collide with neighboring molecules 10^8 times and travel on average 140 nm per cantilever oscillation cycle [57]. These fast dynamics imply that hydration layers displaced by a slowly approaching tip are continuously restored upon retraction of the tip – the process is quasistatic. These relatively fast relaxation times ($\sim \text{ps}$) suggest that a nanoscopic hydration experiment should be highly adiabatic. However, we are aware that our experiment is not completely adiabatic even before approaching the surface, as 35 fW of power are necessary to maintain the cantilever at constant amplitude. This power is dissipated into the bulk liquid by viscous loss across the full surface area of the cantilever and tip. The contribution from our nanoscopic tip apex to this non-adiabatic process is on the order of 10^{-23} watts, assuming a tip area of $\sim 1 \text{ nm}^2$. Given some oscillatory density profile of water molecules near a surface, one can expect an oscillatory dissipation profile of roughly 10^{-23} watts. For two reasons the measured dissipation is much larger: the dynamical properties of water molecules change near the interface, and the tip interacts with the surface.

Our detection threshold is $\sim 10^{-17}$ watts. A tremendous change in dynamical properties of water molecules would be necessary to increase the dissipation from 10^{-23} watts to a detectable level. Molecular dynamics simulations predict very modest changes in the translational and rotational dynamics of water [58] until confinement separations of about 0.6 nm are reached [59]. Recently, Watkins *et. al.* used molecular dynamic simulations to demonstrate that the interaction in a nanoscopic AFM hydration experiment can be broken down into “direct” and “water mediated” interactions with the surface [60]. Direct interactions are similar to the short-range interactions that occur in UHV environments. Water mediated interactions have an oscillatory component which can extend up to $\sim 1 \text{ nm}$ from the surface. These sources of dissipation fail to explain the monotonic increase in dissipation which we observe beyond 2 nm away from the surface in our experiment.

The fact that our tip apex is tethered to an overhanging mesoscopic tip structure cannot be ignored, as suggested by Figure 22. Squeeze-film damping of the mesoscopic tip structure can cause a noticeable rise in dissipation in a nanoscopic experiment, which can be approximated as [54]

$$\gamma_{film} \approx \frac{6\pi\eta R^2}{h + h_0}, \quad (33)$$

where η is the viscosity, R is the radius of the mesoscopic tip, h is the height of the nanoscopic tip above the surface, and h_0 is the difference between the mesoscopic and the nanoscopic tip heights. Figure 23a shows the result of fitting our dissipation profile with a squeeze-film damping contribution. Arbitrarily setting $h_0 = 2$ nm returns a tip radius of 50 nm – on the order of what is expected. Three facts warrant the removal of this background dissipation from consideration in our nanoscopic experiment: 1) from our previous discussion, a slow-varying monotonic increase in dissipation is not expected to occur at the apex of a sharp tip; 2) this background dissipation persisted throughout the day of imaging, even after multiple tip crashes and large changes in observed force profiles; 3) it is on the order predicted by squeeze-film damping for a typical mesoscopic tip structure.

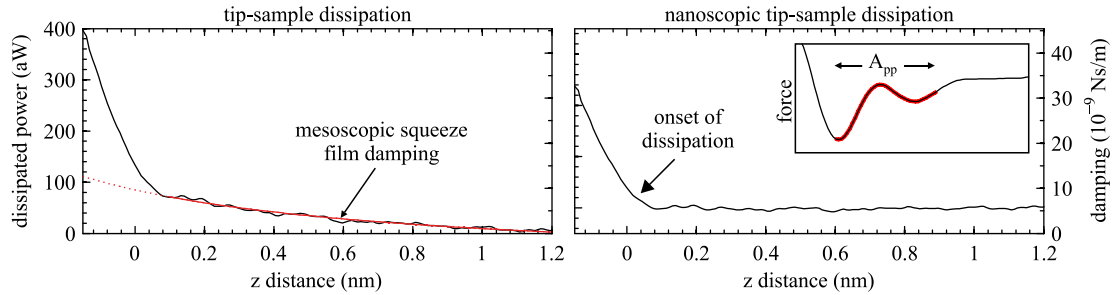


Figure 23: a) Tip-sample dissipation contains a slowly increasing background due to squeeze-film damping caused by an overhanging mesoscopic tip, on the order of what is expected from a typical AFM tip. Removing this instrumental artifact isolates the nanoscopic dissipation profile, which shows a sudden onset of dissipation at $z \sim 0$ nm. This corresponds to the distance at which the tip encounters the strongest attractive force with the hydration layer, at the lowest point of its oscillation. This scenario is illustrated in the inset, along with the peak-to-peak amplitude of the oscillating cantilever in red (the force curve was taken from Figure 17). Both y-scales apply to both images, although an offset was added to the data on the right for plotting purposes only.

Subtracting the effects of squeeze-film damping from our data results in the nanoscopic dissipated power, shown in Figure 23b. A sudden onset of dissipation is observed near $z = 0$ nm. The short-range of the dissipation profile is indicative that it relates to interactions involving only the tip apex. The sudden onset of dissipation coincides with the situation where the tip apex encounters the most attractive force at the bottom of its oscillation cycle, as shown in the inset. It also coincides with the height

which offers the strongest contrast in the frequency shift map, as seen by the xy-plane shown in Figure 21.

4.2.4 Determination of tip-sample distance

The spacing of the observed structure matches the pseudohexagonal lattice of the underlying mica [22]. However, it is unclear *a priori* whether the mica surface or a hydration layer is being imaged. Recent Monte Carlo simulations [18] and molecular dynamic simulations [59] suggest that the lateral distribution of water molecules exhibits long-range order up to the third hydration layer, above which water displays mostly bulklike properties. Both the first and second water layers share a considerable portion of their hydrogen bonds with the highly structured mica surface [18]; they are only 0.1 nm apart and can appear as one layer in an AFM experiment [22]. We will consider them as a single layer in the following discussion, where we determine the absolute tip-sample distance by analyzing additional hydration maps.

In Figure 24, two additional hydration maps are displayed alongside of the data from Figure 21 which is now labelled hydration map A. In hydration map B, the tip successfully displaced an underlying hydration layer, as can be deduced from the force profile. The three cross-sections show that lateral long-range order in the distribution of water molecules was observed in the frequency shift channel at three distinct heights. This information indicates that the onset of dissipation, observed in both hydration maps A and B, coincides with an attractive interaction between the tip and the first/second hydration layer. Furthermore, another regime of strong dissipation appears once the tip attractively interacts with the underlying mica. This dissipation profile *might* be the sum of a short-range direct interaction and a long-range water mediated interaction, however such a distinction is difficult to make experimentally. Although we do not observe an oscillatory dissipation component as one might expect from a water mediated interaction, its existence below our detection threshold cannot be excluded.

In hydration map C, the tip approached the mica up to a repulsive interaction, providing us with a more direct measure of the tip-sample distance. Interestingly, a minor tip change near the end of the scan strongly affected the force profile shape around the first/second hydration layer. A similar effect occurred in map B (not shown). Although these tip changes greatly affected the imaging quality and force profiles, we refer to them as “minor” because they modified the tip-sample distance by no more than 30 pm in both cases. Recent molecular dynamics simulations [60] demonstrated how slight changes in tip geometry can have large effects on the observed force profile. In this

respect, control or characterization of the AFM tip shape is necessary for turning AFM into a more accurate metrological tool.

The cross-section taken just above the mica surface in map C shows detail which could not be readily distinguished in the cross-section of the first/second hydration layer, as indicated by the dotted circles. These features are caused by local electrostatic variations due to the random substitution of Si by Al on the mica surface [61], as well as the presence potassium ions [62]. Unfortunately, hydration map C was acquired after switching from photothermal to piezoacoustic excitation of the cantilever, preventing the measurement of a dissipation profile. In Section 3.2.4, we demonstrated that recovering such a dissipation profile using piezoacoustic excitation is impossible if the temperature of the liquid cell varies by as little as 40 mK throughout the experiment.

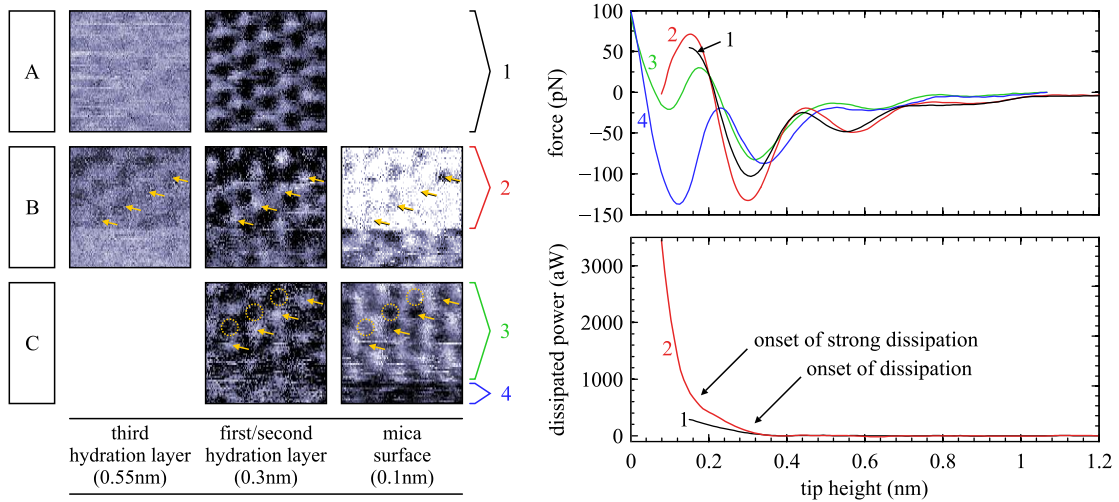


Figure 24: The frequency shift hydration map from Figure 21, labeled A, is shown along with two other three-dimensional hydration maps (B and C), all acquired within one hour. The xy cross-sections were taken at different tip heights; all were separately contrasted for visual ease. The first/second hydration layer was displaced by the tip in data B, allowing it to interact with the mica surface. The arrows aid the eye for observing the contrast inversion between adjacent images. In hydration map C, the tip reached a repulsive interaction with the mica surface. The circles show areas where local variations in the mica surface can be seen. Spectroscopy data corresponding to the images are plotted on the right. The overlaid force profiles reveal that the onset of dissipation occurs when the tip begins interacting with the first/second hydration layer, and that an onset of stronger dissipation occurs upon attractive interactions with the mica surface.

The new FM-AFM theory derived in Section 3.2, which requires a detailed instrumental characterization involving the measurement of transfer functions and modelling the cantilever damping by Sader hydrodynamics, allowed us to unequivocally recover a monotonic damping profile in nanoscopic hydration experiments at the mica-water interface. This study reconciles the debate over monotonic versus oscillatory damping profiles, the root of which has not only been the existence of instrumental artifacts, but also due to the improper comparison between systems of varying length-scales. Whereas oscillatory damping is expected in certain mesoscopic liquid confinement experiments, accurate instrumental characterization of our system reveals a monotonic damping in our nanoscopic hydration experiment.

Beyond proper instrumental characterization, an additional correction was necessary to isolate the damping signal that occurs only at the nanoscopic tip area. This was performed by subtracting the squeeze-film damping from the overhanging mesoscopic tip area. The nanoscopic damping signal carries two strong signatures that can be used to determine the absolute tip-sample distance in future experiments. Conversely, the oscillatory conservative force profile remains an ambiguous measure of tip-sample distance. The onset of dissipation (observable above our detection limit ~ 1 nNs/m) occurs upon interaction with the first/second hydration layer which is caused by large changes in rotational and translation dynamics of water molecules as predicted by simulations. The onset of strong dissipation (when damping exceeds ~ 100 nNs/m) occurs upon direct interaction with the mica surface and was shown to result in unstable tip configurations.

The methodology presented here can aid the determination of tip-sample distance which is necessary for direct comparison to simulations and provide complementary information regarding the physical properties of water molecules probed in nanoscopic hydration experiments.

5. Solvation structures of ionic liquids at the gold interface

The first AFM studies of ionic liquid solvation structures as a function of applied potential were performed in 2011 [63,64]. The experiments were performed alongside electrochemical measurements and STM imaging to help interpret the data. Electrochemical methods observe mean-field effects, such as overall dynamics of the double layer, but cannot probe ionic distributions, while scanning tunneling microscopy (STM) serves as imaging tool for the gold surface or the adsorbed layer of cations or anions. AFM data provide additional information regarding the distribution of IL molecules perpendicular to the surface, their orientation, and their mechanical properties (stiffness and damping).

In the following subsection, the electric double layer theory is extended to ionic liquids, with a literature summary of current research IL electrochemistry theory. The choice of ionic liquid for our study is justified with respect to its properties and research to date. We then explore the electrochemical properties of [BMIM][PF₆] using cyclic voltammetry. Finally, force spectroscopy at the Au(111) surface as a function of electrochemical potential is presented, and compared to a recent study of the same system using static AFM.

5.1 Ionic liquid electrochemical theory

Ionic liquids differ from typical electrochemical systems in that they are supersaturated electrolytes. There is no solvent - only ionic charge carriers exist.

1 kg of water corresponds to 56 moles of water molecules. Even for a 1 M solution, considered a strong concentration, there are almost 30 water molecules for each solute ion-pair. These water molecules screen adjacent charges from each other, effectively reducing interionic interactions. For these reasons, the “non-interacting assumption” used for the EDL theory derivation in the last section was at least qualitatively justifiable.

In contrast, 1 kg of an average ionic liquid corresponds to ~5 moles of ionic pairs, i.e. a ~ 5 M solution. More importantly, interionic interactions inevitably occur because there are no solvent molecules to screen the adjacent charges. In other words, there are strong ionic correlations that govern the behavior of the system. Opposite charges attract, thereby forming an alternating lattice. The liquid nature of ILs makes them best described by a lattice-gas model.

These heuristic arguments justify the need for a complete rederivation of electrochemical theory, which led to the three pioneering works of Kilic *et al.* [24], Kornyshev [25], and Oldham [26] – all published in 2007. The following two subsections provide a derivation more accessible to the broader audience, with approximations made according to the context of this thesis.

5.1.1 Statistical mechanics of the ionic liquid EDL

The theoretical background for the ionic liquid EDL is identical to the EDL derived in Section 4.1.1 for aqueous environments. To reiterate, the Poisson equation governs the electrostatics, while Boltzmann statistics account for thermal fluctuations.

The resulting Poisson-Boltzmann equation for IL differs only by two mathematical constraints imposed on the charge carriers:

- 1) The concentration of total charge carriers is fixed, because either a cation or an anion must exist at any distance x from the solid interface (*i.e.*: there are no solvent molecules):

$$\rho(x) = \rho_-(x) + \rho_+(x) = 2\rho_0. \quad (34)$$

Note that both ρ_- and ρ_+ are positive values in this context.

- 2) Boltzmann statistics determine the probability of interchanging cations and anions by

$$\frac{\rho_-(x)}{\rho_+(x)} \propto e^{2\tilde{\psi}(x)}. \quad (35)$$

where the factor of two exists because an interchange implies both taking a ions from x to ∞ , and inevitably taking a counterion from ∞ to x . (no void in between ions)

Both of these mathematical constraints summarize the ionic correlations of an ideal IL. Inserting these two equations into the Poisson equation (Eq. (26)) results in the IL Poisson-Boltzmann equation:

$$\frac{d^2\psi(x)}{dx^2} = -\frac{2\rho_0 \cdot \tanh(\tilde{\psi}(x))}{\varepsilon}. \quad (36)$$

Note that this equation differs from the aqueous version only by a $\sinh \rightarrow \tanh$ replacement thanks to the beauty of mathematical symmetry. Both functions are plotted in Figure 25 and are very similar for values below 1 (*i.e.*: $\psi < \psi_T$). Once the thermal potential is exceeded, electric fields take control of the ionic concentrations which grow without bound in aqueous solutions (\sinh), but saturate almost immediately in ionic

liquids (tanh). The full concentration profiles $\rho_-(x)$ and $\rho_+(x)$ are also plotted to contrast the behaviour of both liquids.

Note that this simplified model does not capture the charge-density waves expected for an ionic liquid. In fact, this is the limitation of using a mean-field theory to describe a system dominated by steric effects between ions of finite size near a solid boundary. As admitted by Oldham himself [26], such a model is rather naïve for exactly this reason. Nevertheless, this model captures the qualitative behavior of differential capacitance of ILs, as described in the next section.

Before proceeding, it is worth asking why this steric regime, which inevitably also occurs in aqueous solutions at high surface potentials, had thus far remained unexplored in the realm of theoretical electrochemistry. According to Federov and Kornyshev [65], any predictions made about the steric regime in regular electrolytes had thus far been overshadowed by faradaic processes in any experimental setting. With the emergence of ionic liquids, the steric corrections to the Gouy-Chapman theory can be experimentally observed at low potentials well before the onset of faradaic reactions. Yet, strangely, Kilic et al. [24] derived their theory in the broader context of concentrated electrolytes, with no specific mention of ionic liquids...

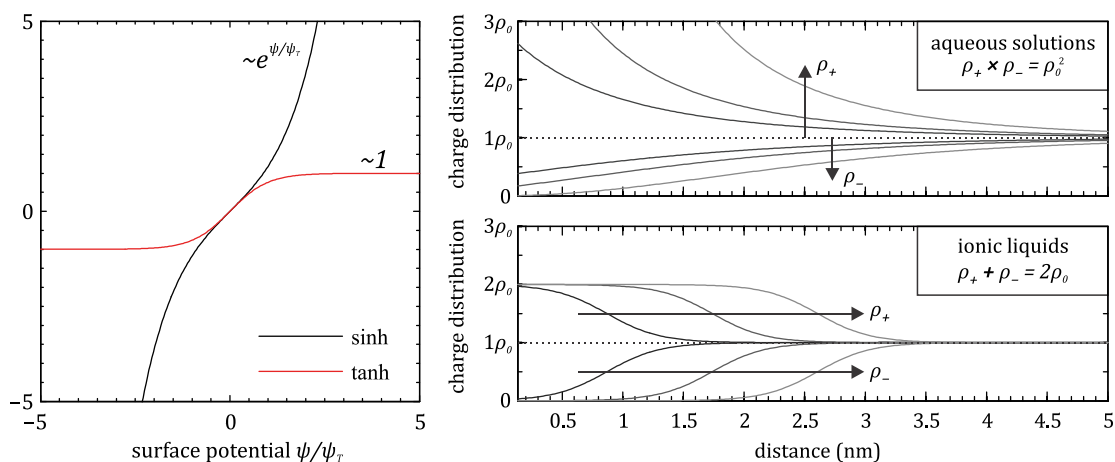


Figure 25: The sinh and tanh function are drawn for reference. The saturation of the tanh function at $\gg 1$ is a result of the strong upper bound on the concentration of the ionic liquid. In the case of aqueous solutions, the geometric mean of ρ_- and ρ_+ is constant for any x , whereas for ionic liquids, the arithmetic mean is constant. The arrows indicate the result of an increase in surface charge.

5.1.2 Differential capacitance of ionic liquids

In the context of cyclic voltammetry, studied in the next section, the differential capacitance of the SLI is of interest, rather than the exact charge carrier distribution

$\rho(x)$. In essence, a large differential capacitance is indicative of better screening capabilities of the solution to surface charges. The differential capacitance can be extracted without solving the Poisson-Boltzmann equation, by noting that $C = \left| \frac{\partial \rho}{\partial \psi} \right|_{x=0}$ such that the specific distribution of $\rho(x)$ need not be known.

In dilute aqueous environments,

$$C_{GC}(\psi) = C_D \cdot \cosh \tilde{\psi}. \quad (37)$$

The reader is reminded that the Debye capacitance $C_D = \varepsilon/\lambda_D$, where $\lambda_D = \sqrt{\frac{\varepsilon\psi_T}{2\rho_0}}$. This result is central to aqueous electrochemical theory; it predicts a differential capacitance *minimum* at the potential of zero charge (PZC), defined as $\tilde{\psi} = 0$, with an exponential dependence for surface potentials in either positive or negative directions.

In ionic liquids,

$$C_{IL}(\psi) = C_D \cdot (\cosh \tilde{\psi})^{-2}. \quad (38)$$

This is a shocking result for an electrochemist, as it predicts a differential capacitance *maximum* at the PZC, with a strong exponential fall-off on either side. Prior to 2007, countless references based their conclusions about ILs on the assumption that the differential capacitance minimum represents the PZC. Their conclusions are sketchy, to say the least.

The equivalent to the Stern-correction exists in the context of ionic liquids. Whereas the Stern-correction fixes deviations at high surface potentials in the Gouy-Chapman theory of aqueous solution, it fixes deviations around the point of zero charge in ILs. The corrected capacitance at the PZC equals $\varepsilon/(\lambda_D + r)$ and converges to Eq. (38) at high potentials.

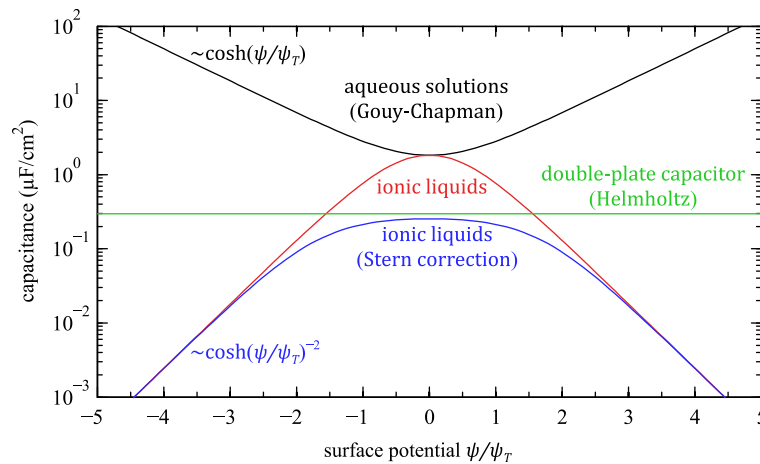


Figure 26: First order result for the differential capacitance of aqueous solution vs ionic liquids. Eq. (37) and (38) are plotted. The Stern correction is applied to the ionic liquid prediction; it only affects the capacitance close to the potential of zero charge.

Note that the derivation leading to Eq. (38) is a severe oversimplification of current IL theory. The works of Kilic *et al.*, Kornyshev and Oldham, are orders of magnitude more sophisticated and complicated. Just as the Gouy-Chapman model predicts an explosion in differential capacitance above a few 100 mV, the IL model presented here predicts an extremely rapid drop to zero capacitance beyond a few ψ_T . The model presented here should serve only to qualitatively describe the difference between aqueous electrolytes and ionic liquids, i.e. the differential capacitance inversion.

One noteworthy approximation used in the model presented here is the consideration of only translational degrees of freedom per charge carrier. In ionic liquids, every charge is associated with a large molecule which possesses multiple degrees of freedom. Every degree of freedom stores thermal energy, and therefore the effective ψ_T parameter of an ionic liquid may be several hundred mV, rather than the 25.7 mV assumed here. Interestingly, the presence of these additional degrees of freedom explains why room-temperature ionic liquids are in fact liquid at room-temperature.

Despite its simplicity, the first order derivation so far uncovers the root of the problem afflicting a decade of IL electrochemical studies. Yet as expected, it still fails to predict most electrochemical observations. Even in aqueous environments, where the ions are mostly screened by water molecules, the exact shape and molecular charge distribution of each ion plays a role in the electrochemical properties of the SLI. Needless to say, the physical properties, such as shape and compressibility, and molecular charge distribution within the anions and cations of an IL will have tremendous impact on their electrostatic and steric interactions.

5.1.3 Corrections to first order theory

The IL EDL derivation in the previous section intrinsically assumed incompressible ions. However, due to their complex molecular structures, ILs can have a high degree of compressibility, relative to aqueous solutions. The compressibility of ILs allows their total charge concentration at the SLI to increase for an applied potential. In other words, the differential capacitance of a compressible IL can see a rise on either side of the PZC, and subsequently decrease at larger surface potentials once the IL lattice saturates. This is illustrated in Figure 27. Note that this behavior has a strong similarity to the original Gouy-Chapman EDL theory, where the concentration also increases at the SLI for an applied voltage.

Kornyshev had already included the concept of compressibility in his pioneering work of 2007 [25] by introducing the compressibility factor

$$\gamma = \frac{2\rho_0}{2\rho_{max}}, \quad (39)$$

where $2\rho_{max}$ represent the maximum concentrations of charge carriers. This γ parameter tunes the EC theory anywhere between the Gouy-Chapman limit of infinitely compressible ions ($\gamma = 0$) and the hard sphere model ($\gamma = 1$) described in the previous section.

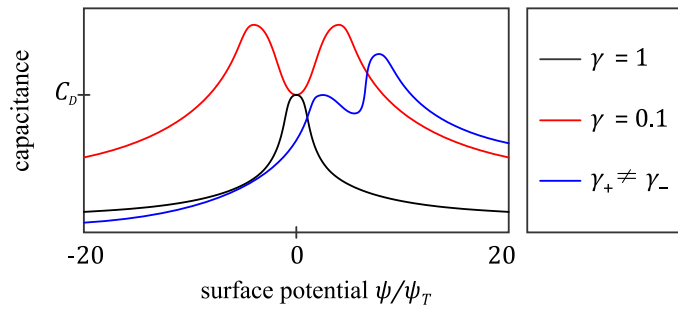


Figure 27: Bell-shaped and camel-shaped curves observable in ionic liquid differential capacitance measurements. These curves may also be asymmetric for cation—anion pairs with differing sizes and/or compressibilities. This plot is not mathematically accurate; it is a visual representation of a plot in [25].

In addition, Kornyshev’s model allows a different compressibility for anions and cations, $\gamma_+ \neq \gamma_-$. Note that simply a difference in size between anions and cations can also be expressed as an asymmetry in *effective* compressibility, stemming from the definition of Eq. (39). Understandably, any asymmetry between the ions translates into an asymmetry in the differential capacitance curves. The increasing capacitance will extend to higher potentials for the polarity at which the more compressible ion is drawn towards the surface. It should be noted that an asymmetry in compressibility causes a shift in the differential capacitance minimum or maximum away from the PZC, as illustrated in Figure 27.

The camel-shaped differential capacitance curve seen in Figure 27 has become a topic of research in many groups. Alternative explanations have been proposed to describe this phenomenon. Trulsson *et al.* modeled the [dispersion forces](#) in ILs and determined that they can cause a local minimum in differential capacitance around the PZC by effectively lowering the cohesion of the liquid molecules to the solid surface [66]. Lauw *et al.* describe how local variations in the dielectric constant near the SLI, due to the specific polarizability of different IL species, can also cause a camel-shaped capacitance [34].

Just recently, Kornyshev's group introduced short-range Coulomb correlations into their models, which predicts overscreening effects at the SLI [33]. In short, overscreening occurs if the first liquid-layer delivers more charge than necessary to screen the solid-surface charge, leading to subsequent opposite screening in the second liquid-layer, etc. In doing so, Kornyshev has further broadened the gap between the EDL as seen by the photochemical and electrochemical communities, as is discussed in the next section.

To summarize this subsection, many hypotheses exist for the observed changes in IL differential capacitance curve from bell-shaped, to camel-shaped, to any asymmetric shape. Future experiments will require complementary techniques and innovative methods for isolating all the possible parameters.

5.2 Ionic liquid selection criteria

Thousands of room-temperature ILs have been synthesized to date, with another million as predicted potential candidates. Our choice for selecting [BMIM][PF₆] ([1-butyl-3-methylimidazolium hexafluorophosphate](#)) and [BMIM][BF₄] ([1-butyl-3-methylimidazolium tetrafluoroborate](#)) for this study is justified in this section. Scientific popularity was the strongest factor in formulating our choice. In fact, the discussion in the next section is made possible due to the extensive number of prior studies based on these two ILs.

[BF₄]⁻ and [PF₆]⁻ based ionic liquids form a group of ILs that do not chemically react with water, although they may absorb water from their environments which can affect their physical and chemical properties [67].

Their composition can be seen in Figure 28.

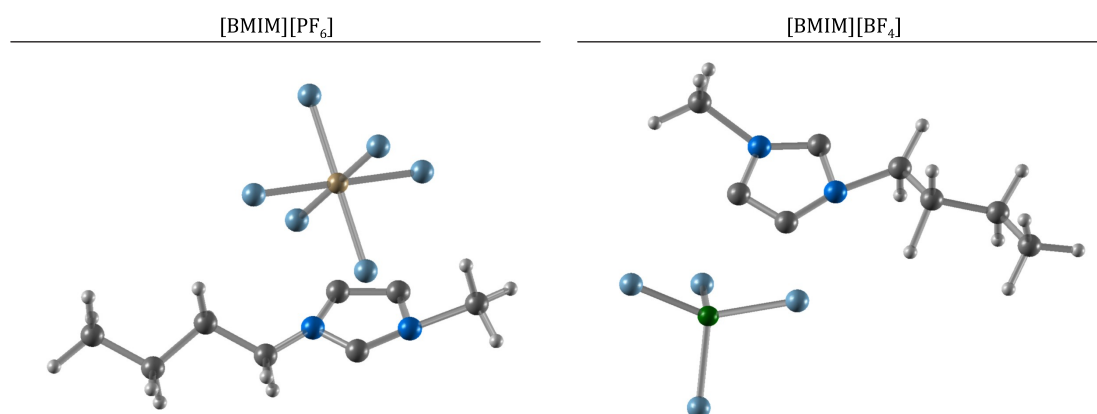


Figure 28: Molecular structures of the [BMIM][PF₆] and [BMIM][BF₄] ion pairs. Click image to enable 3D viewing.

The [BMIM] cation is very tunable due to available functional groups, contributing to its appeal as a subject of scientific study. It forms an ionic liquid with numerous anions, and therefore can serve as a base for future technological applications.

Our study ended prematurely due to time constraints, allowing only the investigation of [BMIM][PF₆] on Au(111). However, all of our initial justifications for selecting both ILs are listed here for completion.

5.2.1 Current scientific arena

The EDL of [BMIM][BF₄] and [BMIM][PF₆] has been widely studied by the photochemical community by means of X-ray photoelectron spectroscopy (XPS) [30,31] and sum frequency generation spectroscopy (SFG) [32,68], amongst others, as described in [69]. These techniques measure a reorientation of the [imidazolium ring](#) at potentials negative to the PZC. The spherical symmetry and negligible compressibility of both [BF₄]⁻ and [PF₆]⁻ anions should lead to unambiguous identification of the predicted reorientation of [BMIM]⁺ using AFM. Also, certain effects of the anions on the AFM measurement could have been isolated by repeating studies in both [BF₄]⁻ and [PF₆]⁻ ILs.

Some of these photochemical results also suggest that the screening lengths are on the order of 0.3 nm and 0.5 nm for [BMIM][BF₄] and [BMIM][PF₆], respectively [68]. In other words, these studies predict that the EDL structure is single-layered. This is contrary to the theoretical work of Kornyshev [33,65], which predicts overscreening effects in ILs that lead to an EDL structure that is actually oscillatory and can extend a few layers into the bulk, as described in Section 5.1.3. In this context, AFM can provide a valuable channel of experimental information to probe the extents of double layer screening near the SLI by direct force measurements.

It has been suggested that molecularly resolved [scanning tunneling microscopy](#) (STM) images of [BMIM] are only attainable on Au(100), and not on Au(111) [29,69]. The STM imaging was complemented by EIS, revealing bell-shaped differential capacitance curves for both [BMIM][BF₄] and [BMIM][PF₆] on gold. These combined studies reveal that electrochemical observations are blind to rich structural information regarding the specific interactions between ILs and the gold substrate. Long-range surface reconstruction and electrochemical annealing of the underlying Au(111) and Au(100) surfaces were observed in [BMIM][BF₄]. A reduction product of [BMIM]⁺ at the cathodic limit is deemed responsible for the annealing process. Additionally, synergistic effects with [BF₄]⁻ near the surface and the structure of the overlaying EDL may play a

role, yet such observations remain out of reach for STM studies that are limited to short tip-sample distances. Such studies can be complemented by the force imaging capabilities of AFM that enables the probing of multiple ionic liquid layers.

5.2.2 *Experimental feasibility*

To the author's [available knowledge](#), all ionic liquids of scientific interest are transparent – a prerequisite for any AFM experiment on our system.

The range of mass densities of most ILs falls within roughly a factor of two: 0.7 – 1.6 g/cm³. From an AFM consideration, lower mass density is beneficial as it maintains a higher cantilever resonance frequency; however, the square root dependence to mass density is rather weak.

On the other hand, the range of viscosities for available ILs spans several orders of magnitude. The viscosity of a single IL can change by an order of magnitude for as little as 10 °C change in temperature. Our choice of [BMIM][PF₆] was initially worrisome because the high reported viscosity $\eta > 300$ mPa · s (300 × more viscous than water) can lead to difficulties in interpreting dynamic AFM results. In fact, our derivation of the massless model of cantilever dynamics in overdamped environments [8] stemmed from this choice, yet it led to the surprising conclusion that AFM calibration becomes easier as η increases.

In retrospect, [BMIM][PF₆] is a poor candidate for AFM studies as it breaks down into [hydrofluoric acid](#) (HF) which dissolves any oxide that it encounters. The quartz rod that holds our cantilever suffered the consequences. [BMIM][BF₄] is expected to be much more stable, and therefore probably represents a better candidate for future studies.

In conclusion, disregarding highly toxic/corrosive by-products, the full spectrum of ionic liquids contains feasible candidates for static and dynamic AFM experiments. Appropriate cantilevers should be chosen for either $Q \gg 1$ or $Q \ll 1$ to avoid the awkward $Q \sim 1$ regime in the case of dynamic AFM.

5.3 *Cyclic voltammetry*

[Cyclic voltammetry](#) (CV) was performed at the [BMIM][PF₆]-Au(111) interface under anhydrous and anaerobic conditions in a dedicated sealed liquid cell equipped with Pt reference and Pt counter electrodes, using a [CH instruments](#) (1000A) potentiostat. The sample preparation and purification of the ionic liquid are described in Appendix 7.1.

Due to its infancy, IL electrochemistry does not yet possess standard reference electrodes, making different datasets difficult to compare reliably, even on the same

instrument because of drift in the quasi-reference electrode. We quote a recent study (2010) by Kolb's group to illustrate this problem [28]:

"We used three different types of electrodes as references: Pt wires, Ag wires coated with AgCl or AgPF₆. The former two, in fact, were quasi-reference electrodes; the third one was a reference electrode of second kind (assuming that the yellowish layer formed on the wire upon anodization in BMIPF₆ was indeed AgPF₆). We found none of these reference electrodes superior to the others; adjusting the potential scale with the different reference electrodes was made on the basis of a characteristic cathodic peak [...]"

In the following cyclic voltammetry (CV) investigation, the same characteristic cathodic peak described above was used as reference. The potential drifted during and in between experiments typically by a few hundreds mV, within a total span within 500 mV throughout all experiments. Potentials are quoted with respect to the Pt quasi-reference electrode.

Three electrochemical regimes were broadly identified by our study of [BMIM][PF₆], which make up the topics of the following subsections.

5.3.1 The double layer regime

The double layer regime is roughly 1.5 V to 2 V wide, and is delimited by a sharp increase of current density beyond the full range of 10 $\mu\text{A}/\text{cm}^2$. It is typically centered between 0 V and +0.5 V depending on RE drift. Staying within this window results in highly reproducible CVs which have full current density ranges within a few $\mu\text{A}/\text{cm}^2$, as observed in Figure 29. These currents represent the charging of the interface caused by displacement and rearrangement of ions, with no associated chemical changes to the IL. A cathodic peak can be observed around 0 V with a broad anodic counterpart. This is consistent with observations made by Gnahn et al. [28,29]; our current densities are just below their reported results (within a factor of two).

According to their extensive [electrochemical impedance spectroscopy](#) (IES) study [29], this central cathodic peak *probably* represents anion-cation replacement at the surface. It was observed that the differential capacitance of the SLI has an asymmetric bell-shape, with larger potentials positive to the PZC, where anions adsorb to the surface. This observation agrees with the Kornyshev model because size asymmetry between both molecules predicts a higher packing density for anions ($\gamma_+ \gg \gamma_-$) leading to a higher capacitance at potentials positive to the PZC. However, the compressibility of either ion is not high enough to cause a camel-shaped differential capacitance curve.

The PZC of their system was determined independently by a method called the immersion technique. More precisely, this method reveals the point of zero *total* charge

(PZTC). Its distinction with the PZC lies in specific adsorptions to the surface. In fact, their experiment revealed that no specific adsorption occurs on either Au(111) and Au(100), making both surfaces nearly indistinguishable from the perspective of [BMIM][PF₆]. As expected, the PZCs differ by 150 mV between both surfaces, which corresponds to their contact potential difference in UHV. The authors conclude that the gold orientation plays little or no role in the electrochemical dynamics of the ionic liquid. This justifies the comparison of our results on Au(111) to their study on Au(100).

Figure 29 represents our (poor) attempt at measuring the differential capacitance of the IL in the absence of a potentiostat capable of EIS measurements. It should be noted that impedance spectroscopy is a difficult technique, and the interpretation of its results can be the topic of an entire doctoral degree. The lack of EIS allowed us only to extract an estimate of the differential capacitance of the system.

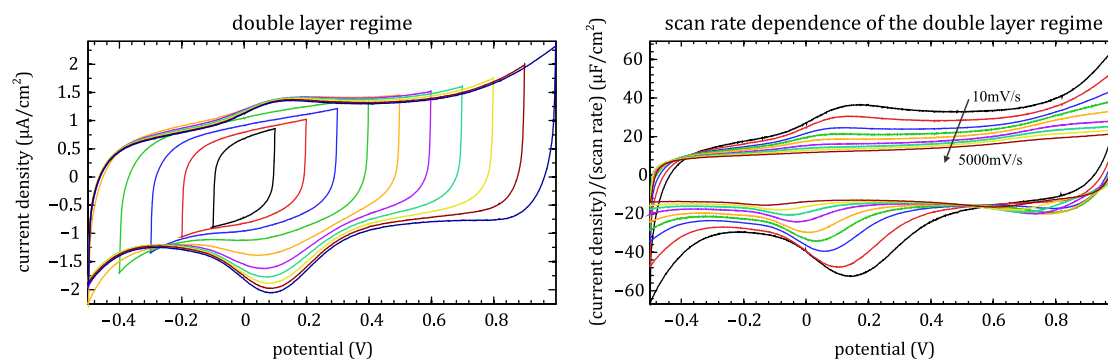


Figure 29: Cyclic voltammetry in the double layer regime for various potential windows, and performed across a large range of scan rates (normalized by the scan rate).

The high frequency limit (fast scan rate) seems to converge to $\sim 10 \mu\text{F}/\text{cm}^2$, which is in good agreement with experiment [29] and theory [25,26]. The potential dependence drops out at high scan rates where the charging process is purely electrostatic in nature.

At low scan rates, the kinetics of the anions and cations near the surface greatly enhance the measured capacitance. A potential dependence of this increased capacitance is observed, as a cathodic peak and a broad anodic counterpart appear near 0 V where anion-cation replacement occurs. We observe a shift in the potential of the cathodic peak of $-0.09 \pm 0.1 \text{ V}/\text{decade}$, which is close to the value observed by Gnahn [28] of $-0.06 \pm 0.1 \text{ V}/\text{decade}$. According to [29], the asymmetry in the peak shapes suggests that the adsorption/desorption of [PF₆] is much slower than that of [BMIM].

In conclusion, despite lacking EIS capability, the results in Figure 29 qualitatively and quantitatively agree with previous results [28,29], as well as with theoretical predictions [25,26]. Interestingly, Kolb and co-workers [29] claim *disagreement* with

Kornyshev [25] and Oldham [26] because their high-frequency capacitance shows no potential dependence, whereas the theorists predict a bell-shaped capacitance. This is a strange assessment as the IL electrochemical theories in question are derived in the quasistatic limit, as described by Oldham in the context of both his and Kornyshev's models:

“The model adopted in the present article is an equilibrium model and it is not equipped to deal with dynamic aspects of the ionic-liquid double layer. In the light of the high viscosity of most ionic liquids, it would be unwise to [...] expect [formulas] to apply to electroanalytical experiments other than those carried out at glacially slow ramp rates or very low frequencies.” [26]

In other words, theoretical predictions should be compared to the low frequency limit of electrochemical observations, as we have done here.

5.3.2 The faradaic regime

Faradaic currents are caused by the reduction or oxidation of the ionic liquid or its by-products. In the context of this study, faradaic reactions are undesirable because they irreversibly affect the composition of the ionic liquid.

As suggested by Figure 30, the faradaic regime extends to a total span of roughly 4 V before the mass transport regime takes over, as is described in the next section. Within faradaic regime are not fully reproducible, vary with time, and affect subsequent experiments performed solely in the double layer regime. The faradaic currents that characterize this window are typically within $100 \mu\text{A}/\text{cm}^2$ for a scan rate of 50 mV/s.

Pseudocapacitive faradaic processes cause the central region of the EC window to grow well beyond the observed current densities observed in the double layer regime. Additionally, irreversible faradaic peaks appear in different locations that depend on the exact potential window being scanned.

We turn to Gnahn and Kolb [70] to explain the strong current excursions that occur beyond ± 1 V:

“A marked increase in the negative current density at around -1.0 V is observed, which is attributed to the reduction of impurities in the ionic liquid, and we assume it is either residual water or it is lithium originating from the synthesis of the IL [...] The anodic current at the positive limit of the potential scan could be due to halide impurities, presumably chloride.” [70]

Performing a CV in the double layer regime immediately after entering the faradaic regime shows currents much higher than previously observed (not shown). These large currents probably represent faradaic reactions with remnant by-products from irreversible faradaic reactions at high potentials. After returning to the double layer

regime, these large currents slowly decay with time and return to their original values of $\sim 1 \mu\text{A}/\text{cm}^2$. However, the peak structure seems permanently affected after entering the faradaic, suggesting permanent changes to the SLI. This observation is consistent with experiments from the group of Kolb [29]; they forbid entering the faradaic regime during their EIS studies for the same reasons. Venturing beyond the double layer regime can also cause permanent potential drift on the order of a few hundred mV, probably due to secondary reactions that occur at the quasi-reference electrode.

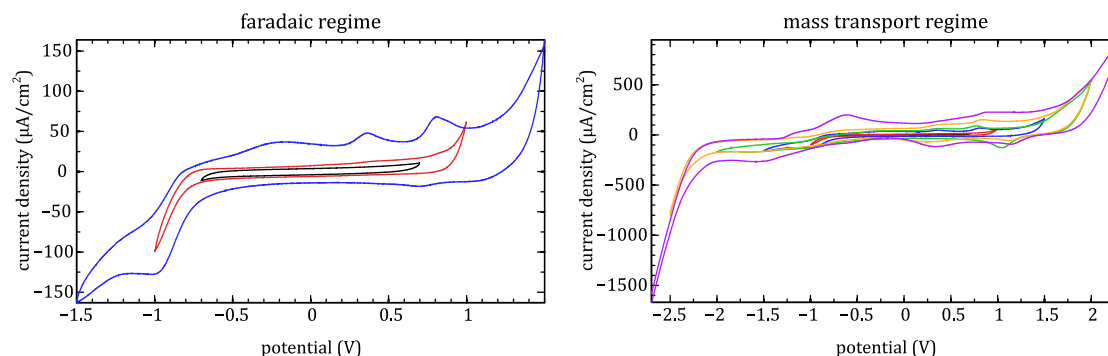


Figure 30: Faradaic and mass transport regimes at increasingly larger potential windows. Note that that current density scale reaches three orders of magnitude more than in the double layer regime from Figure 29.

5.3.3 *The mass transport regime*

A wide electrochemical window beyond the faradaic regime was tested as seen Figure 30b. A sharp increase in current is observed when the potential exceeds the $\sim [-2, 2]$ V window on either side, at which point the IL behavior is dominated by strongly irreversible processes with an ohmic-like electrochemical signature. Note that the current density scale in Figure 30 is $10 \times$ higher in the mass transport regime CV versus the faradaic regime. The ohmic-like resistance in these regions reflects the driven diffusion rates of the IL (referred to as mass transport) from the bulk to the surface where they immediately break down. Below the negative limit, the surge in the current is indicative of cation breakdown. It has been suggested that the radicals created by the process can react with each other and form dimers [71], making this process highly irreversible. A similar complementary process for anions is expected at the positive limit.

Repeated cycling beyond this EC window (on either side) causes irreversible changes to the EC system with catastrophic effects on any CV performed afterwards in the double layer regime. A telltale sign of this irreversibility is that the IL turns brown and opaque.

5.4.1 Imaging the IL/gold interface

A combined static/dynamic AFM imaging technique was used to image [BMIM][PF₆] at the gold interface. The imaging feedback signal was alternated between cantilever oscillation amplitude (dynamic AFM) and cantilever deflection (static AFM) to increase the dynamic range of available imaging setpoints. This technique allowed the imaging of IL layers above the gold surface using dynamic AFM, and subsequent confirmation of the crystallographic orientation of the underlying gold substrate using static AFM.

The phase image of the IL layer suggests a non-uniformity in the IL layer above the Au(111). This *may* be a surface restructuring as previously observed using STM imaging in [BMIM][BF₄] [72], or defects in the IL layer which template etch pits in the underlying gold surface [29,69]. Note that etch pits would not necessarily be observable in the static AFM image, taken immediately after the dynamic AFM image, because of the large contact area in static AFM imaging. Subsequent images taken during CV cycling demonstrate that the features in the phase image are much more prominent when the potential is rising, rather than falling; however, they do not depend on the actual potential within the double layer regime.

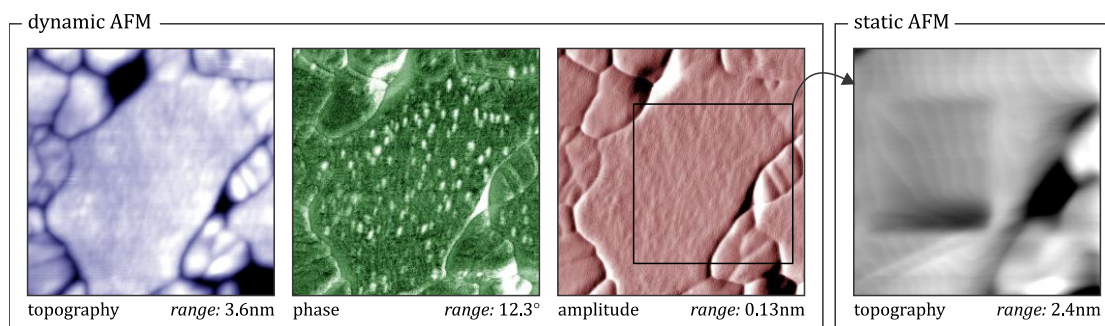


Figure 31: Dynamic (AM) AFM was used to image Au(111) in [BMIM][PF₆]. Gold steps could not be observed as the range of imaging setpoints only allows the imaging of solvation layer above the surface. Switching to static AFM enables the imaging of underlying Au(111) with a 40 nN setpoint; however a 150 nN setpoint damages the surface which can be observed as a square in the image from the previous scan. (image size: 300 nm × 300 nm; scan speed: 5 lines/s; pixel acquisition rate: 5 kHz).

The static AFM image in Figure 31 was acquired at a setpoint of 40 nN, immediately after a smaller scan (seen as the damaged area) was performed at 150 nN. Not surprisingly, static AFM imaging at such high loads destroys the gold surface, as the onset of wear can occur at forces as low as 15 nN in aqueous friction force microscopy on gold [2].

5.4.2 Force spectroscopy of the IL solvation structure

Due to the finite size of IL molecules, there is obviously an oscillatory density profile which extends away from the surface. The debate however is centered around the extent of the screening length to surface charges by ionic liquid molecules at the SLI. Some authors seem to confuse the distinction between an oscillatory density profile, which unequivocally extends several nanometers away from the surface with an exponential-like decay, and an EDL thickness, which can be defined as the effective screening distance to surface charges.

It is necessary to observe a repeatable oscillatory density profile near the surface to confirm that the tip and surface are stable before starting the experiment. Two hundred approach curves were acquired within the span of 100 seconds and exhibited stable behaviour ([see movie online](#)). This experiment was performed at open circuit potential (~ -0.2 V). Immediately after, additional datasets (also 200 averaged approach curves) were acquired at different applied potentials, as seen in Figure 32.

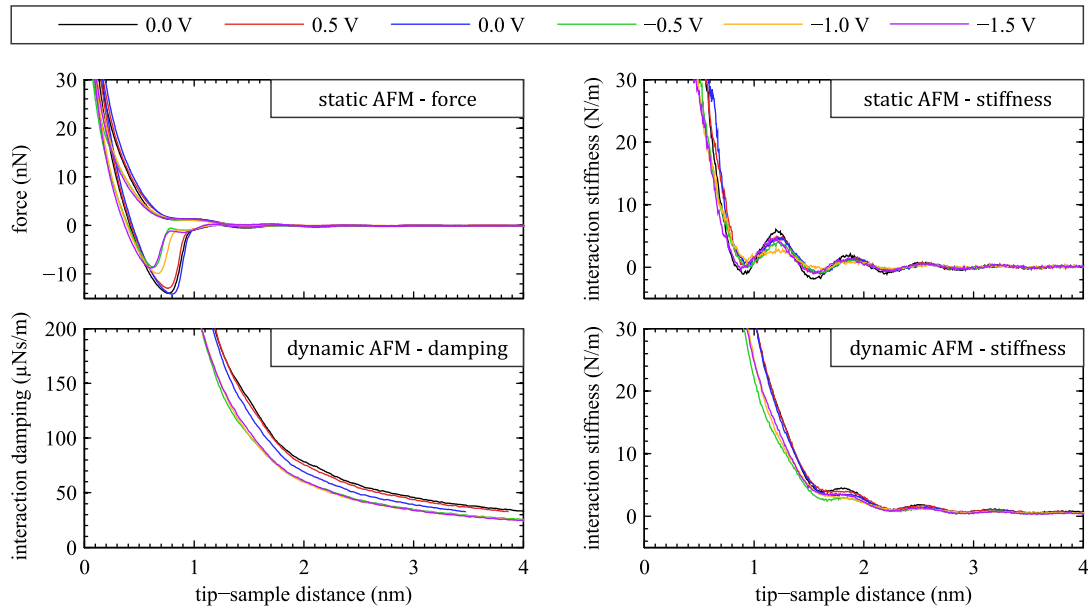


Figure 32: The static force, dynamic damping, and static and dynamic stiffness profiles are shown. The retract curve was also plotted in the force profile, to provide an estimate of the tip-sample adhesion. All curves are the average of 200 approach-retract cycles acquired by simultaneous static and dynamic AFM, where the average deflection, the amplitude, and the phase are measured. Dynamic damping and stiffness were computed using the AM-AFM theory summarized by Eq. (9). Note that the data acquired at -1.5 V represent the first excursion beyond the double layer regime; the potential was kept within the ± 0.8 V until then.

Although there are subtle differences between these datasets, they did not exhibit any correlation with applied potential. In other words, the variability at a given potential exceeded the variability between different potentials. Nevertheless, this dataset is worth investigating, as we can extract an upper bound to the effects of a changing applied potential on the oscillatory profiles of [BMIM][PF₆] at the gold interface – in our experiment.

Very recently, Zhang et al. performed static AFM force spectroscopy of [BMIM][PF₆] at the Au(111) interface using a softer cantilever, and observed a strong potential dependence of the force required to penetrate the last two layers [73]. The potential-dependence of the penetration force spans more than an order of magnitude across the double layer regime with force ranging 1-15 nN, increasing rapidly away from the PZC. This is at variance with our results, which show no potential dependence, with an upper bound of a few 10 % set by the variability in our data.

Averaging the retraction force profile provides a visual estimate of the average adhesion for each dataset, as seen in Figure 32. The tip-sample adhesion decreased at negative potentials.

Differentiating the force profile with respect to tip-sample distance provides a measure of the interaction stiffness. Here, no correlation with applied potential existed up to the last layer of IL.

The dynamic AFM stiffness profile differs from the static AFM stiffness profile significantly for the few layers closest to the gold. This occurs because our assumption that the cantilever can be described as a simple harmonic oscillator, made during the derivation of AM-AFM theory, fails once the interaction stiffness becomes comparable to the cantilever stiffness. The cantilever used here was calibrated in Figure 13 ($k = 28.5$ N/m; $\gamma_s = 120$ μ Ns/m), such that the interaction stiffness reaches > 10 % of the cantilever stiffness upon interaction with the last 2-3 layers. At this point, the cantilever is only accurately described by a combination of pinned and unpinned eigenmodes [46]. A driven pinned cantilever has a shape very different from a driven unpinned cantilever; therefore, the sensitivity (V/nm) changes throughout the approach to the surface.

The problems described in the last paragraph also puts into question the slight oscillatory component in the damping profile, believed to be an instrumental artifact for the same reasons. A stiffer cantilever is required to resolve these issues.

Nevertheless, the dynamic AFM method provides accurate measurements of the damping and stiffness profiles for layers further than 2 nm in our experiment. It can be seen that these profiles also suggest no clear potential dependence of the solvation structure. Note that both damping profiles taken at 0 V show nearly as much variability

as throughout the entire experiment. These differences are likely explained by small changes in the tip structure, which are expected due to the large loading forces (tens of nN).

A common problem when imaging in liquids is the determination of the tip-sample distance. The situation becomes much more problematic in viscous ionic liquids at the gold electrode as the last liquid layer may require very large pressures to be displaced by the tip. Therefore, there is no clear force regime between the liquid removal, and the compression and damage of the gold electrode; i.e. there is no hard-contact regime which can be used to zero the tip-sample distance, as suggested by the inexistence of a linear region in the contact portion of in the static force curve in Figure 32. In fact, it is possible that the gold surface and the tip undergo significant deformation before the last liquid layer is displaced. This observation is consistent with the low damage threshold (somewhere between 40 nN and 150 nN) of the gold sample observed in Figure 31. Given these complications, the tip-sample distance in Figure 32 is poorly defined and somewhat arbitrary.

Using [Hertzian contact mechanics](#), a [back-of-the-envelope calculation](#) for a 100 nm radius spherical indenter into a planar gold surface at 40 nN results in an elastic indentation of ~ 0.1 nm. The sample deformation is expected to be even larger for a sharper tip. In other words, the tip-sample distance is a combination of the sample displacement, the cantilever deflection, as well deformation of the tip and the sample. The deformation of the tip and the sample are quantities that are difficult to model, and nearly impossible to measure, preventing the determination of the true tip-sample distance. The recent paper by Zhang et al. [73] suggests that the [BMIM][PF₆] layers at the gold interface are all 0.55 nm thick, except for the last layer which is 0.45 nm thick. It remains unclear, however, whether the outstanding 0.1 nm is caused by sample deformation, IL reorientation, or a combination of both.

6. Conclusions and Outlook

6.1 Conclusions

Although the detection noise afflicting the optical beam deflection method obeys strict fundamental limits set by optical shot noise, additional system-specific classical noise sources may dominate and should be measured empirically [15]. Importantly, the calibrated noise for cantilever deflection depends on the properties of the *reflected*, rather than *incident*, light beam, such that the cantilever can have a profound influence on the limits of detection of an OBD system. This fact can be used to reduce detection noise by exploiting cantilever curvature [4] or patterning the cantilever with a diffraction grating [7].

If the detection noise of the system is minimized, the thermal noise sets the fundamental limit of resolution for dynamic AFM in both underdamped (water) and overdamped (ionic liquid) environments. However, this thermal noise can be overshadowed by the influence of tip-sample vibrations in measurements of hydration layers at the water/mica interface – a conclusion drawn from stochastic simulations of tip-sample interactions where the relative contribution of detection, force, and displacement noise were quantified [9]. The dominance of tip-sample vibrations over thermal noise justifies the efforts invested into the design of a very rigid tip-sample junction for reduced external noise coupling in our AFM [1].

In FM-AFM, the transfer function of the excitation system (photothermal or piezoacoustic) must be measured and used for converting the acquired data into meaningful conservative and dissipative force signals [6]. Furthermore, the overhanging mesoscopic tip may contribute a significant damping signal which must be subtracted before interpreting atomic-resolution data. These considerations were carefully applied to the results of a three-dimensional atomic-resolution force spectroscopy experiment at the mica/water interface, in order to extract the first accurate conservative *and* dissipative force profiles of such a system [10]. Damping only becomes observable above the noise floor (~ 1 nNs/m) once the tip begins to interact with the first/second hydration layer, and grows monotonically with an onset of strong dissipation (> 100 nNs/m) that occurs once the tip interacts directly with the mica surface. These observations are consistent with simulations that predict bulk-like water properties for the third water layer and beyond. Accurate dissipation spectroscopy of such a system using piezoacoustic FM-AFM was shown to be practically impossible [6].

Unexpectedly, the complications that affect cantilever calibration in liquid environments due to deviations from ideal harmonic behavior near $Q = 1$ actually disappear in overdamped environments ($Q < 0.5$) [8]. However, the photothermal and piezoacoustic methods of excitation strongly differ in overdamped environments: the

base is fixed for photothermal excitation, resulting in predictable cantilever dynamics, whereas the base moves more than the tip for piezoacoustic excitation by an unprescribed amount making the interpretation of data nearly impossible. These problems were solved by retrofitting our AFM with photothermal excitation [3] to perform dynamic AFM experiments in ionic liquids. Combined static and dynamic AFM was used to extend the dynamic range of forces used for topographic imaging of Au(111) in ionic liquids allowing both the solvation layers and the underlying gold substrate to be imaged. Force spectroscopy was also performed using this combined technique, which unveiled problems with dynamic AFM that appear once the interaction stiffness becomes a significant fraction of the cantilever stiffness.

Given the lack of reference electrodes for ionic liquid electrochemistry, a thorough cyclic voltammetry investigation was necessary to correlate our observations with electrochemical results in the literature. Our investigation of force spectroscopy of [BMIM][PF₆] at the Au(111) failed to reveal any changes in the oscillatory solvation structure as a function of surface potential, despite the low noise of our system. Whereas this result is inconsistent with recently published AFM results [73] that demonstrate a correlation between the mechanical properties of the solvation layer and the electric potential, it is in agreement with photochemical measurements [68] that suggest an EDL below one nanometer.

6.2 Outlook

Atomic force microscopy theory is littered with approximations. A multitude of unverified approximations make many results presented in the literature highly questionable. For example, the stiffness profiles in [BMIM][PF₆] measured by dynamic AFM and static AFM differ considerably because the cantilever was assumed to be accurately described as a simple harmonic oscillator, which is clearly incorrect. More accurate models of AFM cantilever dynamics that include all pinned and unpinned eigenmodes are necessary to reconcile these differences.

Controversies regarding oscillatory versus monotonic dissipation profiles, for example, continue to slow down scientific progress in the field. Accurate models and proper calibration procedures in AFM are necessary to resolve instrumental issues. The effects of higher eigenmodes on the cantilever response, the non-linear effects of non-stationary stochastic noise on deterministic measurements, as well as the tip-shape influence on force spectroscopy - to name a few - must be well understood to confidently interpret data acquired at the solid-liquid interface using AFM. Luckily, such topics are under extensive research by us and many groups that will hopefully provide resolutions to these problems in the near future.

7. Appendix

7.1 Sample preparation

7.1.1 Ionic liquid preparation

BMIM-PF6 (1-Butyl-3-methylimidazolium hexafluorophosphate) was purchased from Merck EMD in “high purity grade” ([#4.91050.0100](#)). 20 mL was transferred into a TraceClean I-Chem Vial (40 mL) and pumped on overnight with a diffusion pump at $< 10^{-6}$ mbar pressure at 80 °C. Molecular sieves (0.3 nm) were purchased from VWR, and pumped over the weekend at 200 °C. Roughly 100 molecular sieves were combined with the ionic liquid. The mixture was pumped on overnight with a diffusion pump at $< 10^{-6}$ mbar pressure at 80 °C. The vial was transferred into an argon-filled glove box without breaking vacuum. The oxygen and water content of the glove box were estimated < 1000 ppm and < 100 ppm using the light-bulb method [74]. The IL was transferred from the vial into a Teflon-glass syringe (cleaned by acetone/ethanol cycling and drying with filtered nitrogen), within 20 seconds of exposure to the argon atmosphere.

Although the purification of our IL by molecular sieving was performed such as described in [70], it did not have any observable impact on our CVs. It is possible that Merck EDM has modified their purification protocol in the meantime, and therefore results are not expected to be identical unless IL from the same bottle is used. Nevertheless, the current densities in Figure 29 fall within a factor of two relative to the study in [75].

7.1.2 Au(111) preparation

In the [McGill microfabrication facility](#), a Si(100) wafer was cleaned in hydrofluoric acid, and then baked at 1100 °C for 60 minutes for the growth of 100 nm of SiO₂. Then, 100 nm of gold was sputtered at room temperature at a rate of 0.4 nm/s, and later baked at 450 °C for 4 min. The thick SiO₂ layer prevents interdiffusion of Si and Au atoms which otherwise form a silicide during the baking at 450 °C used to form Au(111) terraces. The template-stripped-gold (TSG) method [76] was used to transfer the gold layer onto a pre-sputtered gold sample holder.

7.2 Preparation of the instruments

7.2.1 Electrochemical studies

A dedicated EC cell was made, which masks all but the center of the TSG Au(111) surface for electrochemical characterization. The exposed area is $0.080 \pm 0.005 \text{ cm}^2$. The Pt reference and Pt counter electrodes are held in close proximity to the sample ($< 2 \text{ mm}$). Roughly 0.1 cm^3 of IL was injected into the cell, under an argon atmosphere (in the glove box described in 7.1.1), and immediately sealed.

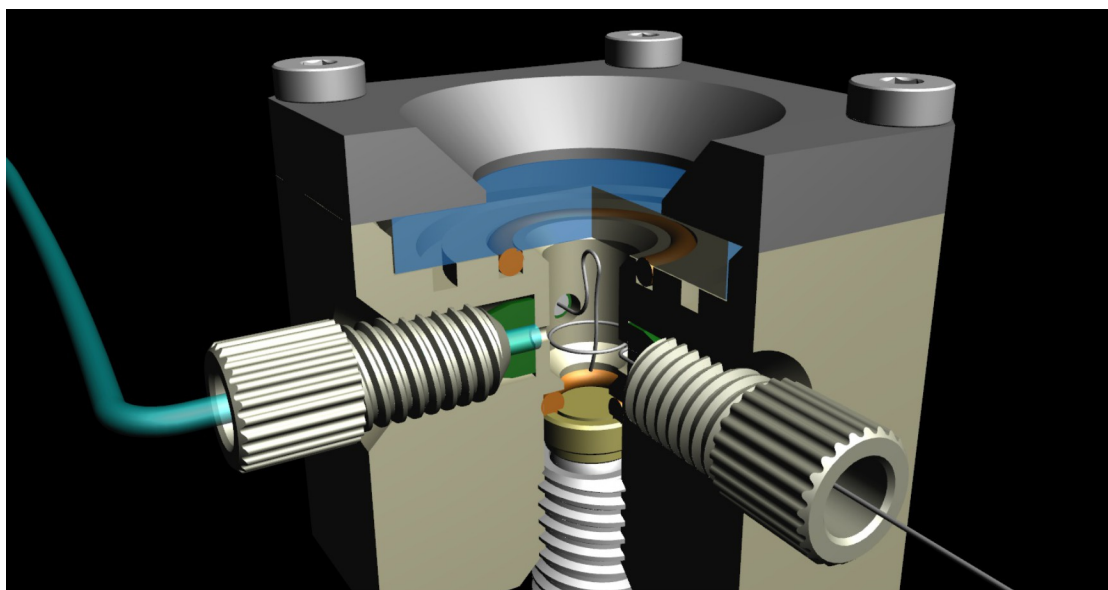


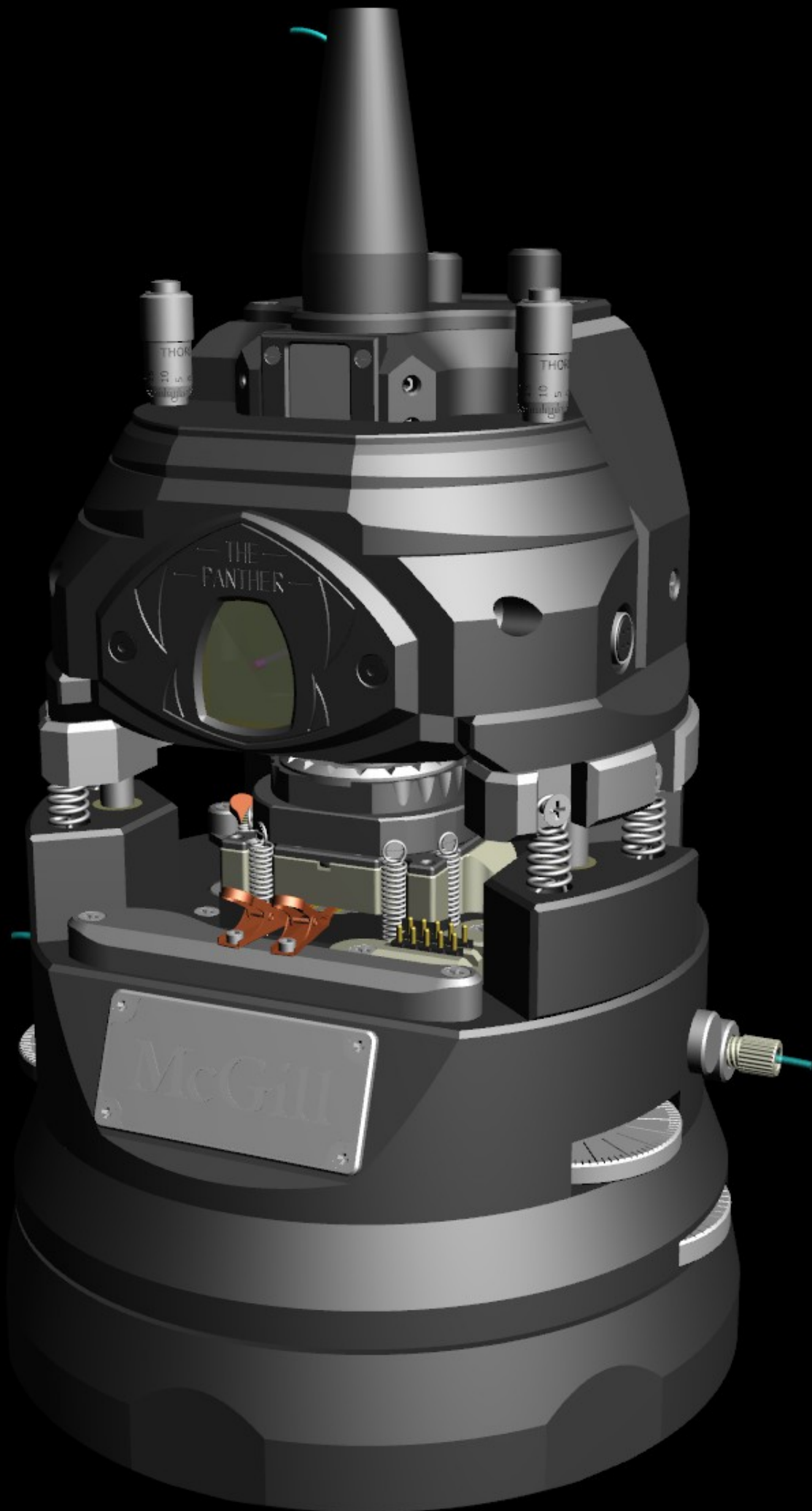
Figure 33: Technical drawing of electrochemical liquid cell. Click figure to enable 3D viewing.

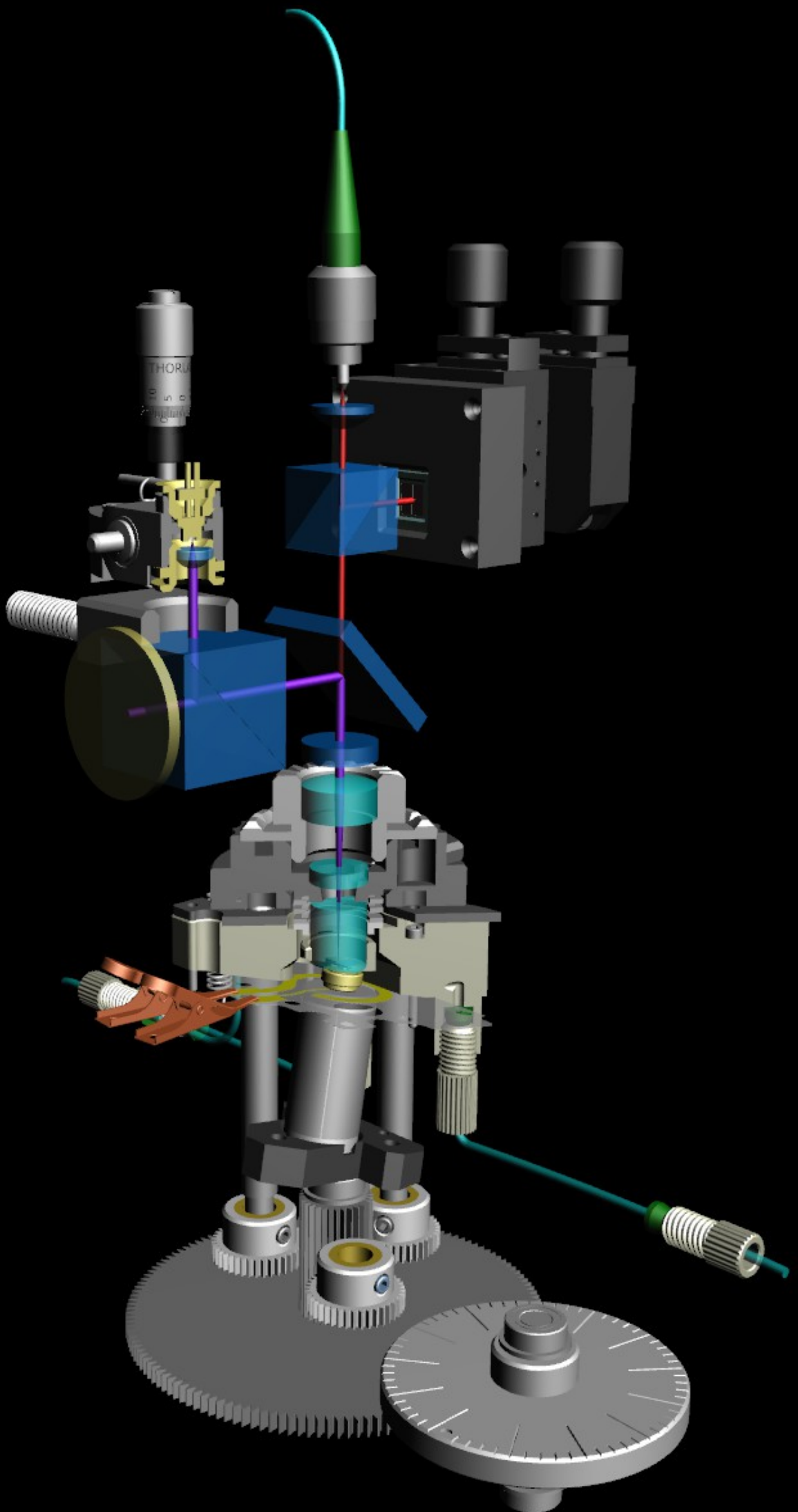
7.2.2 Atomic force microscopy experiments

The liquid cell of the AFM, including a cantilever and gold sample, was sealed. A low pressure stream of argon was used to purge and dry the liquid cell for 30 min. While argon was continuously introduced through the overflow outlet of the liquid cell, at a slight overpressure, IL (prepared in 7.1.1) was injected via the inlet until the liquid cell was nearly full. Then, the argon valve was sealed. The Teflon syringe remained connected to the inlet through the experiment.

7.3 3D interactive technical drawings

Please click on the images on the next two pages to enable 3D viewing. Use *left* button to rotate, *left+right* to pan, *right* to zoom.





8. References

- [1] A. Labuda, W. Paul, B. Pietrobon, R. B. Lennox, P. H. Grütter, and R. Bennewitz, Review of Scientific Instruments **81**, 083701 (2010). ([pdf →](#))
- [2] A. Labuda, F. Hausen, N. N. Gosvami, P. H. Grütter, R. B. Lennox, and R. Bennewitz, Langmuir **27**, 2561–2566 (2011). ([pdf →](#))
- [3] A. Labuda, K. Kobayashi, Y. Miyahara, and P. Grutter, Review of Scientific Instruments **83**, 053702 (2012). ([pdf →](#))
- [4] A. Labuda and P. H. Grütter, Review of Scientific Instruments **82**, 013704 (2011). ([pdf →](#))
- [5] A. Labuda and P. Grütter, U.S. Patent No. Provisional US 61431596 (2011).
- [6] A. Labuda, K. Kobayashi, D. Kiracofe, K. Suzuki, P. H. Grütter, and H. Yamada, AIP Advances **1**, 022136 (2011). ([pdf →](#))
- [7] A. Labuda, J. R. Bates, and P. H. Grütter, Nanotechnology **23**, 025503 (2012). ([pdf →](#))
- [8] A. Labuda and P. Grütter, Langmuir **28**, 5319 (2012). ([pdf →](#))
- [9] A. Labuda, M. Lysy, and P. Grütter, Applied Physics Letters **101** (2012). ([pdf →](#))
- [10] A. Labuda, K. Kobayashi, K. Suzuki, H. Yamada, and P. Grütter, manuscript in preparation (2012).
- [11] A. Labuda, T. Brastaviceanu, I. Pavlov, W. Paul, and D. E. Rassier, Review of Scientific Instruments **82**, 013701 (2011). ([pdf →](#))
- [12] A. Labuda and D. Rassier, U.S. Patent No. US 2011/0271411 A1 (2011). ([pdf →](#))
- [13] A. Labuda, Y. Miyahara, L. Cockins, and P. Grütter, Physical Review B **84**, 125433 (2011). ([pdf →](#))
- [14] A. Labuda, P. H. Grutter, Y. Miyahara, W. Paul, and A. Roy-Gobeil, U.S. Provisional Patent No. US 61/609,994 (2012).
- [15] A. Labuda, M. Lysy, W. Paul, Y. Miyahara, P. Grütter, R. Bennewitz, and M. Sutton, Physical Review E **86** (2012). ([pdf →](#))
- [16] A. Labuda, A. Roy-Gobeil, Y. Miyahara, and P. Grütter, manuscript in preparation (2012).

- [17] E. Cartlidge, *New Scientist* - Feb 6th 32 (2010).
- [18] A. Malani, K. Ayappa, and S. Murad, *The Journal of Physical Chemistry B* **113**, 13825 (2009).
- [19] J. Wang, A. G. Kalinichev, R. J. Kirkpatrick, and R. T. Cygan, *The Journal of Physical Chemistry B* **109**, 15893 (2005).
- [20] L. Cheng, P. Fenter, K. Nagy, M. Schlegel, and N. Sturchio, *Physical Review Letters* **87**, 156103 (2001).
- [21] U. Raviv, P. Laurat, and J. Klein, *Nature* **413**, 51 (2001).
- [22] T. Fukuma, Y. Ueda, S. Yoshioka, and H. Asakawa, *Physical Review Letters* **104**, 2 (2010).
- [23] B. E. Conway, *Electrochemical Supercapacitors* (Plenum Press, New York, 1999).
- [24] M. Kilic, M. Bazant, and A. Ajdari, *Physical Review E* **75**, 1 (2007).
- [25] A. Kornyshev, *The Journal of Physical Chemistry B* **111**, 5545 (2007).
- [26] K. B. Oldham, *Journal of Electroanalytical Chemistry* **613**, 131 (2008).
- [27] T. Oyama, S. Yamaguchi, M. R. Rahman, T. Okajima, T. Ohsaka, and N. Oyama, *Langmuir : the ACS Journal of Surfaces and Colloids* **26**, 9069 (2010).
- [28] M. Gnahn, T. Pajkossy, and D. M. Kolb, *Electrochimica Acta* **55**, 6212 (2010).
- [29] M. Gnahn, C. Müller, R. Répánszki, T. Pajkossy, and D. M. Kolb, *Physical Chemistry Chemical Physics : PCCP* **13**, 11627 (2011).
- [30] T. Cremer, M. Stark, A. Deyko, H.-P. Steinrück, and F. Maier, *Langmuir : the ACS Journal of Surfaces and Colloids* **27**, 3662 (2011).
- [31] J.-K. Chang, M.-T. Lee, W.-T. Tsai, M.-J. Deng, H.-F. Cheng, and I.-W. Sun, *Langmuir : the ACS Journal of Surfaces and Colloids* **25**, 11955 (2009).
- [32] S. Baldelli, *The Journal of Physical Chemistry. B* **109**, 13049 (2005).
- [33] M. Bazant, B. Storey, and A. Kornyshev, *Physical Review Letters* **106**, 6 (2011).
- [34] Y. Lauw, M. Horne, T. Rodopoulos, and F. Leermakers, *Physical Review Letters* **103**, 117801 (2009).
- [35] S. Das and S. Chakraborty, *Physical Review E* **84**, 012501 (2011).
- [36] M. Sha, G. Wu, Q. Dou, Z. Tang, and H. Fang, *Langmuir* **26**, 12667 (2010).

- [37] J. Vatamanu, L. Cao, O. Borodin, D. Bedrov, and G. D. Smith, *The Journal of Physical Chemistry Letters* **2**, 2267 (2011).
- [38] T. Fukuma, T. Ichii, K. Kobayashi, H. Yamada, and K. Matsushige, *Applied Physics Letters* **86**, 034101 (2005).
- [39] A. Research, <http://www.asylumresearch.com/News/News.shtml#PointDefects> (2011).
- [40] G. B. Kaggwa, J. I. Kilpatrick, J. E. Sader, and S. P. Jarvis, *Applied Physics Letters* **93**, 011909 (2008).
- [41] S. O'Shea, *Physical Review Letters* **97**, 179601 (2006).
- [42] A. Maali, T. Cohen-Bouhacina, G. Couturier, and J.-P. Aimé, *Physical Review Letters* **96**, 2 (2006).
- [43] D. Kiracofe and A. Raman, *Nanotechnology* **22**, 485502 (2011).
- [44] J. E. Sader, *Journal of Applied Physics* **84**, 64 (1998).
- [45] K. Blgtekjaer, *Lightwave* **8**, 183 (1990).
- [46] U. Rabe, K. Janser, and W. Arnold, *Review of Scientific Instruments* **67**, 3281 (1996).
- [47] C. P. Green and J. E. Sader, *Physics of Fluids* **17**, 073102 (2005).
- [48] K. Kobayashi, H. Yamada, and K. Matsushige, *Review of Scientific Instruments* **82**, 033702 (2011).
- [49] F. J. Giessibl, *Applied Physics Letters* **78**, 123 (2001).
- [50] S. D. Beer, W. K. D. Otter, D. V. D. Ende, W. J. Briels, and F. Mugele, *Europhysics Letters* **97**, 46001 (2012).
- [51] C. D. F. Honig, M. Radiom, B. A. Robbins, J. Y. Walz, M. R. Paul, and W. A. Ducker, *Applied Physics Letters* **100**, 053121 (2012).
- [52] M. B. Viani, T. E. Schäffer, A. Chand, M. Rief, H. E. Gaub, and P. K. Hansma, *Journal of Applied Physics* **86**, 2258 (1999).
- [53] D. A. Walters, J. P. Cleveland, N. H. Thomson, P. K. Hansma, M. A. Wendman, G. Gurley, and V. Elings, *Review of Scientific Instruments* **67**, 3583 (1996).
- [54] S. Khan, G. Matei, S. Patil, and P. Hoffmann, *Physical Review Letters* **105**, 1 (2010).
- [55] Y. Zhu and S. Granick, *Physical Review Letters* **87**, 096104 (2001).
- [56] K. Kobayashi and H. Yamada, manuscript in preparation (2012).

- [57] C. Sendner, D. Horinek, L. Bocquet, and R. R. Netz, *Langmuir : the ACS Journal of Surfaces and Colloids* **25**, 10768 (2009).
- [58] Y. Leng and P. Cummings, *Physical Review Letters* **94**, 19 (2005).
- [59] Y. Leng and P. T. Cummings, *The Journal of Chemical Physics* **124**, 74711 (2006).
- [60] M. Watkins and A. Shluger, *Physical Review Letters* **105**, 1 (2010).
- [61] A. Malani and K. G. Ayappa, *The Journal of Physical Chemistry. B* **113**, 1058 (2009).
- [62] K. Kimura, S. Ido, N. Oyabu, K. Kobayashi, Y. Hirata, T. Imai, and H. Yamada, *The Journal of Chemical Physics* **132**, 194705 (2010).
- [63] R. Atkin, N. Borisenko, M. Drüschler, S. Z. El-Abedin, F. Endres, R. Hayes, B. Huber, and B. Roling, *Physical Chemistry Chemical Physics : PCCP* **13**, 6849 (2011).
- [64] R. Hayes, N. Borisenko, M. K. Tam, P. C. Howlett, F. Endres, and R. Atkin, *The Journal of Physical Chemistry C* **115**, 6855 (2011).
- [65] M. Fedorov and a Kornyshev, *Electrochimica Acta* **53**, 6835 (2008).
- [66] M. Trulsson, J. Algotsson, J. Forsman, and C. E. Woodward, *The Journal of Physical Chemistry Letters* **1**, 1191 (2010).
- [67] L. E. Barrosse-Antle, A. M. Bond, R. G. Compton, A. M. O'Mahony, E. I. Rogers, and D. S. Silvester, *Chemistry, an Asian Journal* **5**, 202 (2010).
- [68] S. Baldelli, *Accounts of Chemical Research* **41**, 421 (2008).
- [69] Y.-Z. Su, Y.-C. Fu, J.-W. Yan, Z.-B. Chen, and B.-W. Mao, *Angewandte Chemie (International Ed. in English)* **48**, 5148 (2009).
- [70] M. Gnahn and D. M. Kolb, *Journal of Electroanalytical Chemistry* **651**, 250 (2011).
- [71] M. C. Kroon, W. Buijs, C. J. Peters, and G.-J. Witkamp, *Green Chemistry* **8**, 241 (2006).
- [72] L. Lin, *Electrochemistry Communications* **5**, 995 (2003).
- [73] X. Zhang, Y.-X. Zhong, J.-W. Yan, Y.-Z. Su, M. Zhang, and B.-W. Mao, *Chemical Communications (Cambridge, England)* **48**, 582 (2012).
- [74] O. Mao, Z. Altounian, and J. O. Ström-Olsen, *Review of Scientific Instruments* **68**, 2438 (1997).
- [75] T. Pajkossy and D. M. Kolb, *Electrochemistry Communications* **13**, 284 (2011).
- [76] M. Hegner, P. Wagner, and G. Semenza, *Surface Science* **291**, 39 (1993).